

STUDY OF TiO₂ MORPHOLOGIES FOR CdS QUANTUM DOTS SENSITIZED SOLAR CELLS

A Project Report Submitted
as part of the requirements for the degree of

MASTER OF SCIENCE

Submitted by

ANKITA KOLAY

Roll No. **CY14MSCST11003**

Under the Supervision of

DR. M. DEEPA



भारतीय प्रौद्योगिकी संस्थान हैदराबाद
Indian Institute of Technology Hyderabad

To the

**DEPARTMENT OF CHEMISTRY
INDIAN INSTITUTE OF TECHNOLOGY HYDERABAD
INDIA**

APRIL, 2016

Declaration

I hereby declare that the matter embodied in this report is a result of investigation carried out by me in the Department of Chemistry, Indian Institute of Technology Hyderabad under the supervision of **Dr. M. Deepa**.

In keeping with general practice of reporting scientific observations, due acknowledgement has been made wherever the work described is based on the findings of other investigators.

Ankita Kolay

(Signature)

ANKITA KOLAY

(Student Name)

CY14MSCST11003

(Roll Number)



Signature of Supervisor

Dr. M. Deepa

Department of Chemistry

Indian Institute of Technology Hyderabad

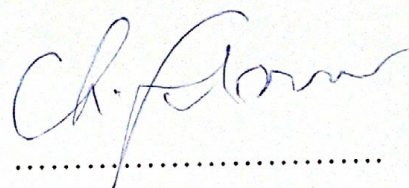
Kandi, Sangareddy- 502285,

Telangana, India.

Dr. M. Deepa
Head & Associate Professor
Department of Chemistry
Indian Institute of Technology Hyderabad
Kandi, Sangareddy, Telangana, India

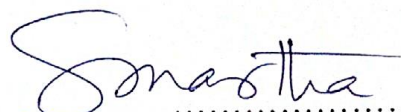
Approval Sheet

This thesis entitled “Study of TiO₂ Morphologies for CdS Quantum Dot Sensitized Solar Cells” by Ankita Kolay is approved for the degree of Master of Science from Indian Institute of Technology Hyderabad.



.....
Name and affiliation

Examiner



.....
Dr. SURENDRA K. MARTHA

Assistant Professor Name and affiliation

Department of Chemistry Examiner

Indian Institute of Technology Hyderabad



.....
Name and affiliation

Advisor

Dr. M. Deepa
Head & Associate Professor
Department of Chemistry
Indian Institute of Technology Hyderabad
Kandi-502285, Sangareddy, Telangana, India

Acknowledgements

I would like to express my utmost gratitude to my supervisor, **Dr. M. Deepa**, for her constant support and motivation. I consider it a privilege to have been given the opportunity to work under her exemplary guidance. I am immensely thankful for her invaluable detailed advice and encouragement throughout the course of this project. Her expertise, patience and understanding were instrumental in the successful completion of my research work and in the organization of my thesis.

I would like to thank **Mr. P. Naresh Kumar** for his time and guidance in helping me understand the concepts and techniques of my work, and for his valuable inputs throughout the duration of this project. I also extend my thanks to Mrs. M. Radha, Mr. K. Ramesh, Ms. Aparajita Das and Mrs. Sweta Lal for their assistance and cooperation at all levels of the research project. I also thank my group members, Rajat Verma and Snehasis Bhunia, for their company and support during the course of this work.

I am deeply grateful to my Head of Department, Dr. M. Deepa, and to the entire Department of Chemistry, IIT Hyderabad, for providing this project opportunity and for extending all necessary facilities for the completion of this project.

Lastly, I express my heartfelt thanks to my parents, and Rini, without whose ceaseless moral support and motivation this work could never have been completed.

Abstract

Quantum Dot Sensitized Solar Cells (QDSCs), which employ quantum dots as photon harvesters, have emerged as the most promising candidate among third-generation photovoltaic devices due to their versatility and range of unique features. The proper assembly and ordering of semiconductor quantum dots in a mesoscopic oxide film such as TiO₂ is crucial for the fabrication of efficient QDSCs. In spite of their huge potential in improving the power conversion efficiency (PCE) of solar cells, the photovoltaic performance of QDSCs is found to be limited by two main factors, namely, the charge recombination at the electrode/electrolyte interface, and transport of photogenerated electrons through the nanostructured photoanode architecture. The latter problem may be circumvented by modification and control of TiO₂ morphology, which can play a crucial role in enhancing PCE by directing charge separation and increasing electron mobility. In this work, four different TiO₂ morphologies—TiO₂ nanoparticles, TiO₂ nanowires, TiO₂ nanosheets and TiO₂ nanospheres—have been synthesized and studied as possible TiO₂ substrates for QDSCs. Structural characterizations based on SEM analysis, X-Ray Diffraction, and BET measurements, optical characterizations such as fluorescence and absorption spectral analyses, emission decay as well as cyclic voltammetry, impedance studies and J-V characteristics have been performed. The power conversion efficiency (PCE) of cells constructed with the CdS-sensitized TiO₂ morphologies as photoanodes and with carbon fabric as counter electrode in sulfide electrolyte have been compared, wherein TiO₂ nanoparticles have shown highest efficiency, (~4.67 %), followed by TiO₂ nanowires (~3.72 %), TiO₂ nanospheres (~3.69 %) and TiO₂ nanosheets (~2.99 %).

Contents

List of Figures

List of Tables

1. Introduction.....	1
1.1 Construction and working of a Solar Cell.....	2
1.2 Generations of Solar Cells.....	3
1.2.1 Shockley-Queisser Limit.....	5
1.3 Dye-Sensitized Solar Cells.....	5
1.4 Quantum Dot Sensitized Solar Cells.....	7
1.4.1 Quantum Dots and Quantum Confinement.....	7
1.4.2 Advantages of Quantum Dot Sensitized Solar Cells.....	8
1.4.3 Working principle of a Quantum Dot Sensitized Solar Cell.....	9
1.5 Solar cell efficiency and key parameters.....	11
1.6 Current Status of Quantum Dot Sensitized Solar Cells.....	12
2. Experimental Section.....	20
2.1 Chemicals.....	20
2.2 Synthesis of TiO₂ morphologies.....	20
2.2.1 Synthesis of TiO₂ Nanowires.....	20
2.2.2 Synthesis of TiO₂ Nanosheets.....	21
2.2.3 Synthesis of TiO₂ Nanospheres.....	21
2.3 Preparation of Photoanodes.....	22
2.3.1 Photoanode Preparation for TiO₂ P25.....	22
2.3.2 Preparation of photoanode for different TiO₂ morphologies.....	23

2.4 Electrolyte and Counter.....	23
3. Result and Discussion.....	24
3.1 SEM Analysis.....	24
3.2 XRD Analysis.....	25
3.3 BET and BJH Analysis.....	26
3.4 Fluorescence Spectral Analysis.....	27
3.5 Emission Decay Analysis.....	28
3.6 Absorption Spectral Analysis.....	30
3.7 Cyclic Voltammetry.....	32
3.8 Impedance Studies.....	33
3.9 Energy Band Diagram.....	35
3.10 Solar Cell Characterization.....	36
4. Conclusion.....	37
References	

List of Figures

1.1 A traditional p-n junction.....	2
1.2 Working of a Solar Cell.....	3
1.3 Schematic representation of the working of a Dye-Sensitized Solar Cell.....	6
1.4a Splitting of energy levels in semiconductor, quantum dots and molecule.....	7
1.4b Quantum confinement effect on DOS (density of states).....	8
1.5 Schematic of MEG.....	9
1.6 Schematic representation of the working of a Quantum Dot Solar Cell.....	9
1.7 Redox reactions involving the QDs and the S^{2-}/S_n^{2-} polysulfide electrolyte.....	10
1.8 Schematic drawing of bare QD sensitized nanocrystalline TiO_2 electrode showing (a) four major recombination paths and (b) recombination paths related to trap states in QDs.....	11
1.9 J-V and IPCE curves of a solar cell.....	12
1.10 Type I and Type II Quantum Dots.....	13
1.11 Schematic illustration of the mechanism with (a) ZnS/SiO_2 double barrier and (b) am- $TiO_2/ZnS/SiO_2$ coating inhibiting the charge recombination processes.....	16
1.12 Schematic diagram illustrating the electron transfer (k_{et}) from Mn-doped CdS into TiO_2 nanoparticles with k_r and k_r' representing charge recombination.....	17
1.13 Schematic illustration of vertically aligned (a) TiO_2 nanowires with smooth and branched architectures and (b) TiO_2 nanowire/ ZnO nanosheet hybrid arrays.....	19
2.3.1 Schematic representation for preparation of TiO_2/CdS photoanode.....	22
2.3.2 Schematic representation of different TiO_2 morphologies on FTO.....	23
2.4 Photograph of Carbon fabric pasted on Glass.....	23
3.1 SEM Image of (a) TiO_2 NPs, (b) TiO_2 NWs, (c) TiO_2 NSh and (d) TiO_2 NSp. Insets show the corresponding enlarged view of the different morphologies.....	24
3.2 X-Ray Diffraction patterns of the different TiO_2 morphologies.....	25

3.3 BET analysis plot of the different TiO ₂ morphologies.....	27
3.4 Fluorescence spectra of the different TiO ₂ morphologies with CdS.....	28
3.5 Emission decay for the different TiO ₂ morphologies with CdS.....	29
3.6 Absorption spectra of (a) CdS, (b) TiO ₂ P25; (c) TiO ₂ NW; (e) TiO ₂ NSh; (g) TiO ₂ NSp; Tauc plots for (d) TiO ₂ NW; (f) TiO ₂ NSh; (h) TiO ₂ NSp.....	30
3.7.1 Cyclic Voltammograms of the different TiO ₂ morphologies.....	32
3.7.2 Cyclic Voltammograms of CdS.....	33
3.8.1 Nyquist plot for different TiO ₂ morphologies; Inset: enlarged view of origin.....	34
3.8.2 Bode Phase Plot for different TiO ₂ morphologies.....	34
3.9 Energy band diagram of TiO ₂ /CdS corresponding to the different morphologies.....	35
3.10 J-V curves for different TiO ₂ morphologies with CdS.....	36

List of Tables

1.1 First Generation Solar Cells.....	3
1.2 Second Generation Solar Cells.....	4
1.3 Third Generation Solar Cells.....	4
1.4 Materials for Quantum Dot Solar Cells.....	13
3.1 Major peaks with their corresponding hkl and d-spacing values.....	26
3.2 BET and BJH analysis data for different TiO ₂ morphologies.....	26
3.3 Kinetic parameters of emission decay analysis deduced from biexponential fits.....	29
3.4 Wavelength, change in optical density (ΔOD) and band gap data for different TiO ₂ morphologies and CdS from absorption spectra and Tauc plot.....	31
3.5 Data obtained from Cyclic Voltammograms of different TiO ₂ morphologies and CdS....	33
3.6 Recombination times for different TiO ₂ morphologies.....	34
3.7 Solar cell parameters for the different TiO ₂ morphologies with CdS.....	36

1. Introduction

The Sun provides about 100000 TW to the Earth, which is approximately 10000 times greater than the world's present rate of energy consumption (13 TW).¹ Photovoltaic cells, which can harvest energy directly from sunlight, are being increasingly used to address growing global energy needs.² Photovoltaic technology has the potential to play a crucial role in a sustainable energy future with minimal negative impacts on the environment.

Photovoltaics is the direct conversion of light into electricity at the atomic level. Some materials exhibit a property known as the photoelectric effect that causes them to absorb photons of light and release electrons. The photoelectric effect was first observed by Edmond Becquerel in 1839, and described subsequently by Albert Einstein in 1905, for which he was later awarded the Nobel Prize in Physics. The first photovoltaic module was built by Gerald Pearson, Calvin Fuller, and Daryl Chaplin of Bell Laboratories in 1954, where it was found that silicon gave an electric charge when exposed to sunlight. In the 1960s, photovoltaic cells were used by the space industries to provide power aboard spacecrafts. With further advances in technology, photovoltaic energy has gained recognition as a reliable source of power and finds use in small commercial devices such as watches and calculators, to light homes, and in large scale industrial applications the world over.

Nanoscience has provided new opportunities to harness clean energy by introducing methods to harvest photons with greater efficiency. With the rapid progress in nanotechnology, semiconductor nanocrystals have emerged as new building blocks that can be employed in designing organic and inorganic hybrid structures with enhanced selectivity and efficacy towards light energy conversion.³ Photovoltaic devices have thus undergone a remarkable series of changes, evolving from the initial silicon based solar cells to far more sophisticated devices based on tailored nanostructures. Research on organic photovoltaic devices has also attracted considerable attention in recent years. With these developments in mind, it is necessary to transform the profile of solar power and energy generation by the commercialisation of these optimised third-generation photovoltaics in order to ensure a greener future for our planet while meeting humanity's ever-growing energy demand.

1.1 Construction and working of a Solar Cell

The function of a photovoltaic device is based on the traditional p-n junction. A p-n junction is formed when two types of semiconductors, n-type (having excess electrons) and p-type (having excess holes), come into contact. At this interface, excess electrons in the n-type material diffuse to the p-type side (exposing positive ion cores in the n-type side), while excess holes from the p-type material diffuse to the n-type side (exposing negative ion cores in the p-type side). This results in an electric field at the junction, forming the depletion region. The electric field, in turn, gives rise to a voltage.

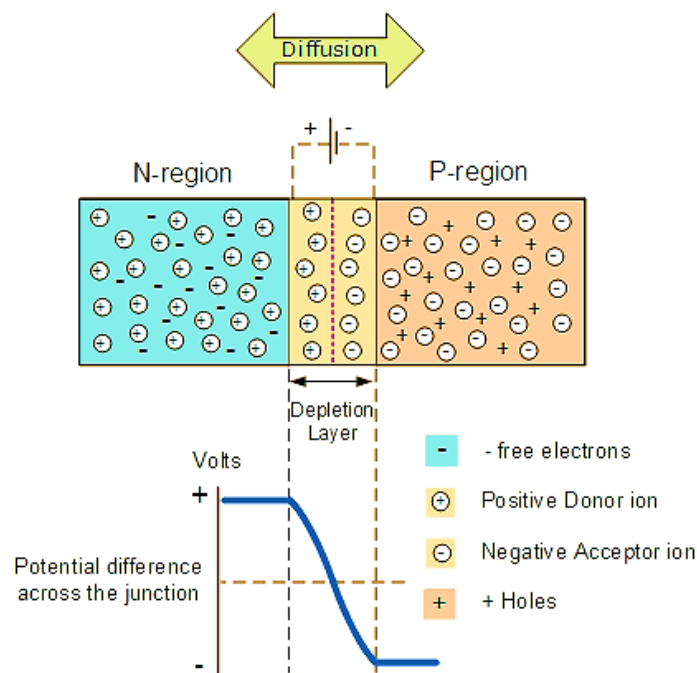


Figure 1.1: A traditional p-n junction.

A solar cell essentially consists of a silicon p-n junction diode with a glass window on the top surface of the p-type material which is made extremely thin so as to allow the incident photons to reach the junction easily. When light falls on the solar cell, a voltage is generated across its terminals, which increases with increase in intensity of radiation.

The generation of current in a solar cell, known as 'light generated current', involves two major processes:

- Photons striking the junction result in the formation of electron-hole pairs. These charge carriers are, however, meta-stable; if they recombine, then no power or current can be generated.

- A second process, therefore, prevents the recombination of these charge carriers by using the electric field generated at the p-n junction to separate the electrons and holes. When the light-generated minority carrier reaches the p-n junction, it is swept across the junction by the electric field existing there, wherein it becomes a majority carrier. Under short-circuit conditions, these carriers flow through the external circuit as light-generated current.

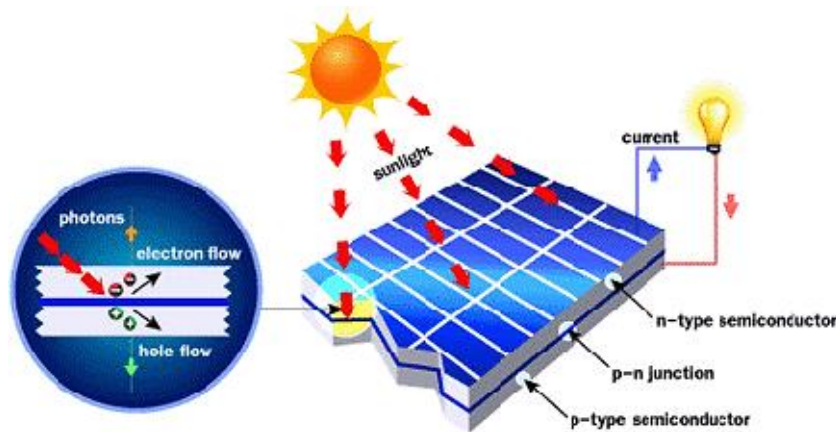


Figure 1.2: Working of a Solar Cell.

1.2 Generations of Solar Cells

Solar cells are often classified according to generations, as first, second and third generation solar cells. The **first generation solar cells**, based on single-crystalline silicon, were capable of delivering sufficiently high efficiencies in the range of 15-20 % (with certified highest efficiency of 25%).⁴

FIRST GENERATION	
Crystalline silicon-wafer based semiconductor	
Advantages	Disadvantages
<ul style="list-style-type: none"> ➤ High carrier mobilities ➤ High efficiency ➤ Commercialized 	<ul style="list-style-type: none"> ➤ Expensive manufacturing technology ➤ Electron-hole recombination is high

Table 1.1: First Generation Solar Cells.

The first generation solar cells, however, came with their own set of complications. These, coupled with the need for cost-reduction, paved the way for **second generation solar cells**.^{5,6} While these were less expensive than wafer-based solar cells, their efficiencies were also found to be lower than those of their predecessors, rarely exceeding 10-15 %.

SECOND GENERATION	
Thin film deposits of semiconductor; Amorphous silicon, Polycrystalline silicon, CdTe, CIGS (Copper Indium Gallium Selenide)	
Advantages	Disadvantages
<ul style="list-style-type: none"> ➤ Lower manufacturing costs ➤ Reduced mass 	<ul style="list-style-type: none"> ➤ Lower efficiencies ➤ Amorphous silicon is unstable ➤ Increased toxicity

Table 1.2: Second Generation Solar Cells.

To overcome these challenges, the **third generation solar cells** aim at high efficiencies and reduced manufacturing costs by using inexpensive, environmentally-benign materials as well as developing cost-effective manufacturing processes. Third generation photovoltaic devices, especially Quantum Dot Sensitized Solar Cells (QDSCs), strive to circumvent the **Shockley-Queisser limit** that limits the theoretical efficiency of single junction solar cells to 31%.

THIRD GENERATION	
Photo-electrochemical cell: CZTS, DSSC, BHJ photovoltaic cells, QDSC and Perovskite solar cells	
Advantages	Disadvantages
<ul style="list-style-type: none"> ➤ No reliance on p-n junction ➤ Higher efficiency due to MEG 	<ul style="list-style-type: none"> ➤ Fabrication cost varies as well as stability ➤ Not yet commercialized

Table 1.3: Third Generation Solar Cells.

1.2.1 Shockley-Queisser limit:

In 1961, William Shockley and Hans J. Queisser showed that a single p-n junction solar cell has theoretical limit of efficiency, known as Shockley-Queisser limit. According to their calculations, the highest power conversion efficiency (PCE) achievable in a single-junction solar cell with a semiconductor absorber having an optimal band gap of 1.1 eV is ~31%.⁷ Size-tunability of band-gap, which is one of the attractive features of QDSCs, can allow for the construction of tandem (two junctions) or multijunction solar cells which have the potential to increase the energy harvested from the broad solar spectrum.⁸ Calculations using the Shockley-Queisser methodology indicate that the maximum theoretical efficiency is expected to increase from 31% to 42% for double-junction solar cells and further to 49% for triple junction architectures.^{4,9}

1.3 Dye-Sensitized Solar Cells

The modern version of a dye solar cell, or Grätzel cell, was originally co-invented in 1988 by Brian O'Regan and Michael Grätzel and later developed until the publication of the first high efficiency DSSC in 1991.¹⁰ Unlike conventional semiconductor devices, dye sensitized solar cells (DSSCs) separate the function of light absorption from charge carrier transport.

A DSSC contains a mesoscopic semiconductor oxide film (usually anatase TiO_2 , but alternative wide-band-gap oxides such as ZnO and Nb_2O_5 may also be used)¹¹ coated with a monolayer of the dye (such as Ru-based N-719, Z-907), which acts as the sensitizer. Current is generated when photoexcitation of the dye results in electron injection into the conduction band (CB) of the semiconductor oxide. The dye is then regenerated by electron transfer from a redox species in solution (such as the I^-/I_3^- couple), which is subsequently reduced at the counter electrode.

The working of a DSSC may be explained by the schematic given in Fig. 1.3.

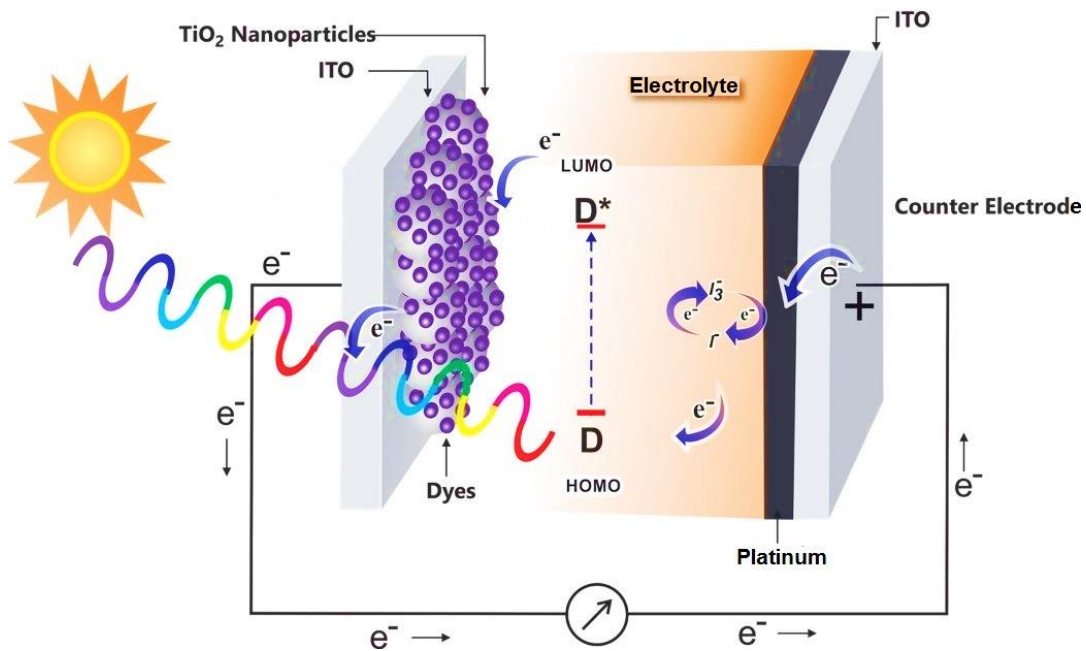


Figure 1.3: Schematic representation of the working of a Dye-Sensitized Solar Cell.

The main attraction of DSSC is that it is the most efficient third-generation solar technology currently available, having achieved upto 12-13 % efficiency till date.^{12, 13} Moreover, they can work efficiently even under diffused light conditions.

DSSCs, however, have certain shortcomings which must be overcome in order for it to commercially compete with current photovoltaic devices.

- X** Firstly, DSSCs suffer from low open circuit voltage due to losses in potential during electron transfer from redox couples to dye molecules.
- X** Secondly, the ruthenium dyes that are generally employed do not absorb in the near-IR region; increase in efficiency would therefore require the utilisation of a broader range of the solar spectrum.
- X** Other problems include the corrosive nature of the iodide electrolyte, possible electrolyte leakage and the expense of the Ru dyes used.

1.4 Quantum Dot Sensitized Solar Cells

A Quantum Dot Sensitized Solar Cell (QDSC) is one of the most promising examples of third-generation solar cells, wherein quantum dots (QDs) are employed as the light-absorbing photovoltaic material. Although they are yet to attain as high power conversion efficiencies as their dye-sensitized counterparts, QDSCs hold great potential due to certain attractive features that have placed these photovoltaic devices in the limelight in recent years.

1.4.1 Quantum Dots and Quantum Confinement

In bulk semiconductors, exciton (electron + hole) pairs move freely in all directions. When the semiconductor length is reduced to the same order as the Bohr exciton radius, quantum confinement effect occurs, i.e., the wave function gets confined to the physical dimension of the particles. Depending on the dimension of confinement, we can have a quantum well, a quantum wire or a quantum dot. A quantum dot is confined in three dimensions; this causes the 'band' of energies to turn into discrete energy levels. The smaller the QD size, the larger the band gap, enabling the tunability of both optical and electronic properties.

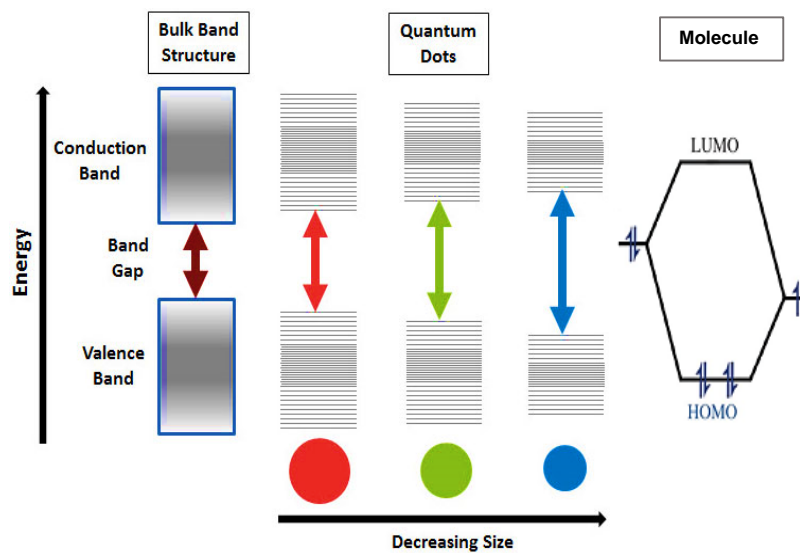


Figure 1.4a: Splitting of energy levels in semiconductor, quantum dots and molecule.

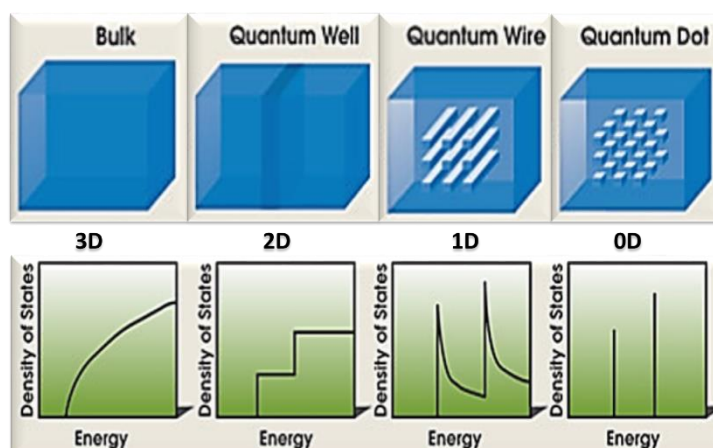


Figure 1.4b: Quantum confinement effect on DOS (density of states).

1.4.2 Advantages of Quantum Dot Solar Cells

QDSCs possess certain unique characteristics that make them stand out among next-generation photovoltaic devices. These include: ^{14,15}

- ✓ The simplicity of the synthetic procedure
- ✓ Tunability of light absorption
- ✓ MEG : Multiple Exciton Generation
- ✓ Sensitivity to diffused light

Simplicity of the synthetic procedure: The preparation of QDs involves little complication, and the QDs may be deposited on the photoanode by drop casting/spin coating¹⁶, electrodeposition/electrophoretic deposition^{17,18}, chemical bath¹⁹ or successive ion layer adsorption and reaction (i.e., SILAR)²⁰.

Tunability of light absorption: The optoelectronic properties of QDs, such as band gap, are a function of their size. It is thus possible to tune the band gap, and therefore the light absorption by the QDs, across a wide range of energy levels by simply controlling or manipulating the particle diameter. The colour of QDs therefore varies with size, with larger QDs (5-6 nm) usually appearing red or orange and smaller QDs (2-3 nm) showing colours like blue or green.

Multiple exciton generation: When the energy of a photon absorbed by a QD is at least twice the bandgap energy, it can lead to the generation of one or more additional excitons instead of being wasted as heat. Conversion efficiency increases as the excess kinetic energy of the electrons and holes creates additional e^-h^+ pairs which can further be separated, transported and collected to yield higher photocurrents in the cell.²¹

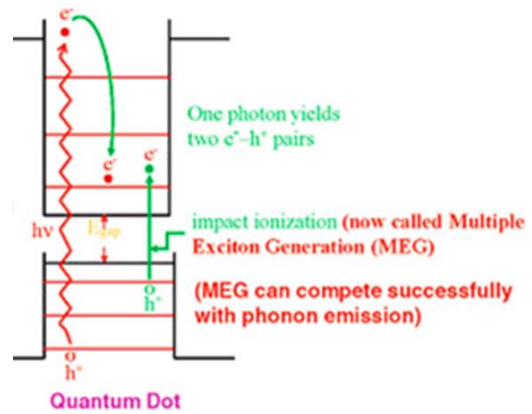


Figure 1.5: Schematic of MEG.

Sensitivity to diffused light: The above properties of bandgap tunability and MEG allow QDSCs to absorb visible light efficiently under diffuse conditions.

1.4.3 Working Principle of a Quantum Dot Solar Cell

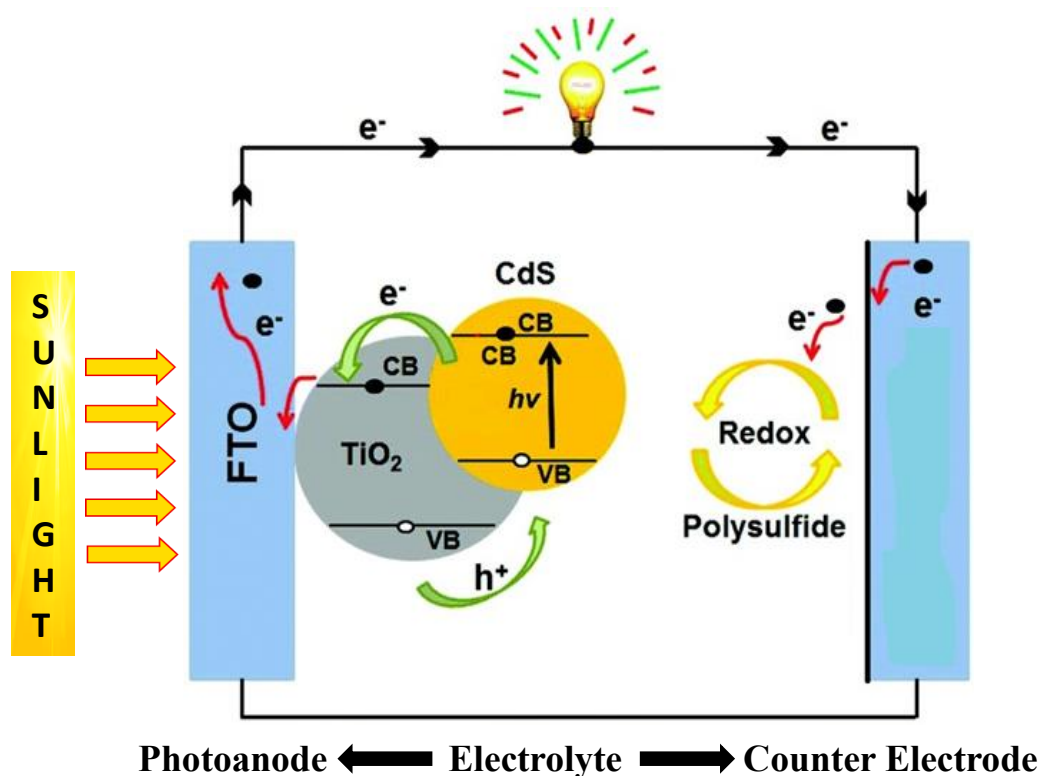


Figure 1.6: Schematic representation of the working of a Quantum Dot Solar Cell.

Photoexcitation of the QD causes bandgap excitation and charge separation, generating electrons and holes. The hole remains in the valence band (VB) of the QD, while the photogenerated electron gets transferred to the CB of a large band-gap semiconductor such as TiO₂. Ultrafast charge injection from excited QD into TiO₂ is followed by quick scavenging of holes remaining in the VB by the redox couple in the electrolyte, in order to lengthen the lifetime of the charge carriers. The oxidized species is then reduced at the counter electrode to regenerate the redox couple, completing the cycle.²²

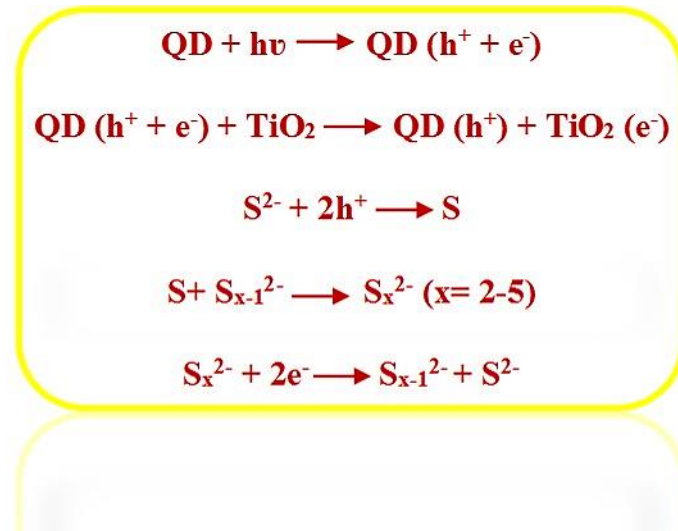


Figure 1.7: Redox reactions involving the QDs and the S²⁻/S_n²⁻ polysulfide electrolyte.

There is a possibility of charge recombination of electrons in the CB of both QDs and TiO₂ at the electrolyte interface, and surface trap state defects which hinders the performance of QDSC. This may occur via four possible pathways as given in Fig. 1.7.²³

1. Internal charge recombination inside QD
2. Excited electron recombination from QD to the oxidized species in electrolyte at QD/electrolyte interface
3. Electrons in the TiO₂ back transfer to QD at TiO₂/QD interface,
4. Direct electron loss from TiO₂ nanoparticles to the electrolyte at TiO₂/electrolyte interface

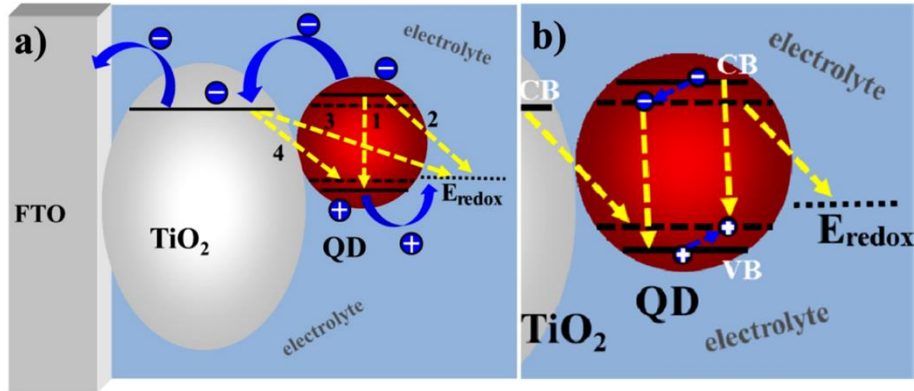


Figure 1.8: Schematic drawing of QD sensitized nanocrystalline TiO₂ electrode showing (a) four major recombination paths and (b) recombination paths related to trap states in QDs.

1.5 Solar cell efficiency and key parameters

The IV curve of a solar cell is the superposition of the IV curve of the solar cell diode in the dark with the light-generated current.

- **V_{oc}:** The *open circuit voltage* of the solar cell is the maximum voltage that the solar cell will supply at zero net current, which is the difference between the redox potential of electrolyte and TiO₂ conduction band.
- **I_{sc}:** The *short-circuit current* is the current through the solar cell when the voltage across the solar cell is zero.
- **FF:** The *Fill Factor* is defined as the ratio of the maximum power from the solar cell to the product of V_{oc} and I_{sc}. It is the area of the largest rectangle which fits in the IV curve.

$$FF = P_{\max} / (V_{oc} I_{sc}) = (V_{\max} \cdot I_{\max}) / (V_{oc} \cdot I_{sc})$$

- **PCE:** *Power Conversion Efficiency* or *efficiency* of a solar cell is determined as the fraction of incident power which is converted to electricity, and defined as the ratio of energy output from the solar cell to input energy from the sun.

$$\text{PCE} / \eta = P_{\max} / P_{\text{inc}} = (V_{\text{oc}} \cdot I_{\text{sc}} \cdot \text{FF}) / (P_{\text{inc}})$$

- **IPCE:** *Incident Photon to Charge Carrier Efficiency* or *Quantum Efficiency (QE)* measures the conversion efficiency of incident light into electrical energy as a function of the wavelength of light impinging on the cell.

$$\text{IPCE}\% = [I_{\text{sc}}(\text{A}) * 1240 * 100] / [P(\text{W}) * \lambda(\text{nm})]$$

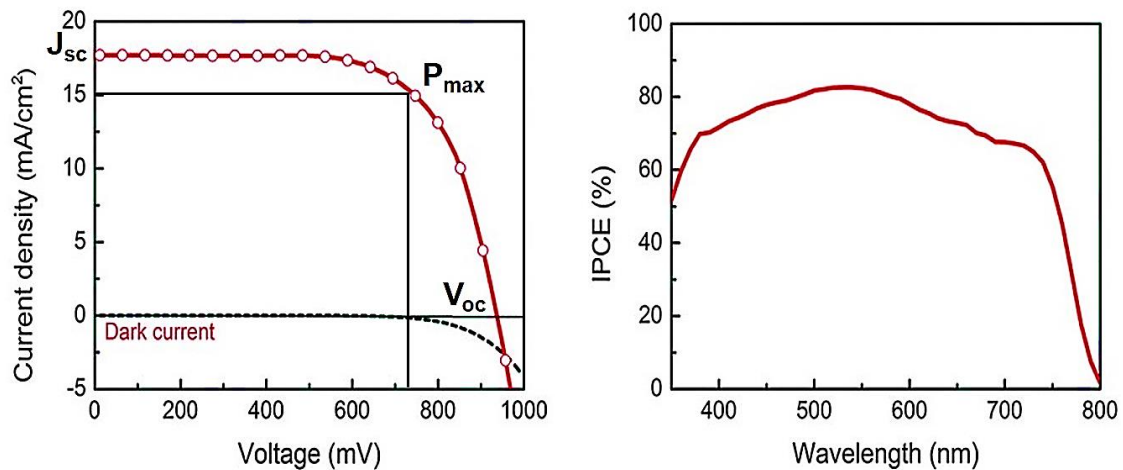


Figure 1.9: J-V and IPCE curves of a solar cell.

1.6 Current status of Quantum Dot Sensitized Solar Cells

Some of the common materials employed as semiconductor, QD, electrolyte and counter electrode in QDSCs are summarized in Table 1.4.^{24, 25}

Semiconductor	Quantum Dots	Electrolyte	Counter Electrode
TiO ₂ , SnO ₂ , ZnO, WO ₃ , etc.	CdS, CdSe, CdTe, PbS, PbSe, Bi ₂ S ₃ , InP, GaAs, CuInS ₂ , etc.	Polysulfide (S ²⁻ /S _n ²⁻), I ⁻ / I ₃ ⁻ , Fe ³⁺ / Fe ²⁺ , Co ²⁺ / Co ³⁺ complexes, etc.	Carbon fabric, Pt, Au, PEDOT, Graphite, RGO, Cu ₂ S, MWCNT, etc.

Table 1.4: Materials for Quantum Dot Solar Cells.

The energy level of QDs employed in QDSCs should match that of wide bandgap semiconductor chosen. Among the quantum dots, Cd chalcogenide QDs are considered most suitable as they are more stable in QDSCs although they may degrade upon visible illumination.²⁶ QDs may be classified into three major types: *core-type*, *core-shell*, and *alloyed quantum dots*.

- ❖ **Core-Type Quantum Dots:** Uniform, single-component materials, such as zinc or cadmium chalcogenides.
- ❖ **Core-Shell Quantum Dots:** Two-component materials where the external shell improves quantum yield by passivating non-radiative recombination sites. In type-I QDs, the energy band gap of the shell material is larger than that of the core material so the electron-hole pair is confined within the core. In type-II QDs, the energy levels of the VB and the CB of core and shell cross each other so some of the electrons are separated from their holes. This is illustrated in Fig. 1.7.

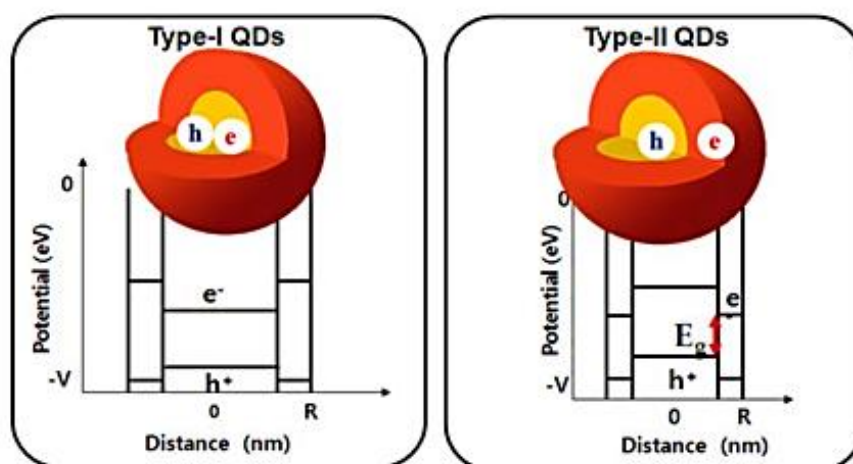


Figure 1.10: Type I and Type II Quantum Dots.

- ☀ A **CdSeTe/CdS Type I core/shell QDSC** has been reported, wherein the CdS shell around the CdSeTe core QD *decreases surface defect density, increases the stability of the core QD and suppresses charge recombination* at the QD/TiO₂/electrolyte interfaces, giving a cell with PCE of **9.48%**, thus showing 13% enhanced efficiency as compared with that of plain CdSeTe QDSCs.²⁷
- ☀ A **CdTe/CdSe Type-II core/shell QD sensitizer** based solar cell with an absorption range extending into the infrared region has been reported, with a record PCE of **6.67%**, which showed *increased electron injection and reduced charge-recombination* as compared to QDSCs based on CdSe sensitizer alone.²⁸
- ❖ **Alloyed Quantum Dots:** Multicomponent materials with gradient composition regions determining the optical and electronic properties of the nanocrystal.

 - ☀ **CdSe_{0.45}Te_{0.55} alloyed QDs** have been designed, which show *high chemical stability and wider absorption range, extending into the near infrared (NIR) region*, relative to the constituents CdSe and CdTe. The resulting alloyed QDs were found to exhibit a PCE of **6.48%**.²⁹
 - ☀ In spite of the focus on cadmium and lead chalcogenide based QDs, the toxicity of these materials are known to pose hazards to human health and environment. Significant efforts are therefore being directed at developing efficient ‘**green**’ QDSCs that do not employ Cd or Pb. An example of such a green QDSC is based on **Type I core/shell CuInS₂/ZnS QDs**, which uses a *broad light-harvesting range extending to NIR, reduces recombination* and gives a PCE as high as **7.04%**.³⁰
 - ☀ **PbS QDs** have emerged as a particularly interesting semiconductor material for QDSCs. With a **band gap of 0.41 eV**³¹, PbS has the potential to harvest photons over a wide absorption range, *extending to NIR*. Its band gap can be tuned by decreasing the size of the PbS nanoparticles to the quantum confinement region. *Band gap tunability of PbS*, in turn, helps in achieving two objectives: firstly, a better match with the optimum absorption band gap is possible and secondly, it allows correct band alignment for the injection of photogenerated electrons into the TiO₂ conduction band.³²

With a band gap in the NIR region, PbS QDSCs are expected to show high photocurrents, J_{sc} , larger than 20 mA/cm^2 . Photocurrent as high as 22.3 mA/cm^2 have been reported in a recent study, where a QDSC based on **PbS/CdS** co-sensitized nanoporous TiO_2 electrodes has demonstrated a **PCE of 4.2%**.³³

Besides photoanodes, choice of suitable counter electrode (CE) as well as electrolyte play crucial roles in improving the PCE of QDSCs.

- ☀ An ideal CE should be a catalytically active material for the electrolyte redox couple and should be compatible with the electrolyte medium. For example, a CE based on a **Cu₂S film on FTO substrate**, when employed in a CdSe QDSC, has been found to exhibit a **PCE of 5.21%** with excellent stability at a working state for 10 hours.³⁴
- ☀ The role of the electrolyte has been demonstrated by employing **polysulfide electrolyte with polyethylene glycol (PEG, 15 wt%) additives**, which *suppress the charge recombination occurring at the $\text{TiO}_2/\text{QDs}/\text{electrolyte}$ interfaces*, showing an increment in PCE from 5.80 % to **6.74%** in CdSe based QDSCs.³⁵

Charge recombination at the $\text{TiO}_2/\text{QD}/\text{electrolyte}$ interface and transport of photogenerated electrons through the nanostructured photoanode network are the two main factors that tend to limit the photovoltaic performance of QDSCs. Strategies for enhancing the power conversion efficiency of QDSCs are therefore aimed at:

- Suppressing the charge recombination, either by passivation of the recombination sites, or by metal doping, and
- Designing electrodes with a higher degree of order, in order to improve the electron transfer rates.

Recombination control by passivation

- ☀ The passivation approach has been used to *reduce interfacial recombination* processes in QDSCs by treating the QD-sensitized photoanode with a sequential **ZnS/SiO₂ double layer**. These inorganic overcoating layers act as barriers, inhibiting back recombination at the oxide surface, and increasing cell stability (such as by protecting QDs from corrosion due to electrolyte). By adopting this approach, **CdSe_xTe_{1-x} QDSCs** were found to exhibit a certified record efficiency of **8.21%**.³⁶

- In a further modification of this approach, introduction of an **amorphous TiO₂ (am-TiO₂) buffer layer** at the interface between the QD sensitized photoanode and the ZnS/SiO₂ barrier layer, via a classical TiCl₄ hydrolysis treatment, has been found to boost the effectiveness of the double layer barrier by *remarkably reducing the charge recombination at the photoanode/electrolyte interface*. A CdSe_{0.65}Te_{0.35} based QDSC constructed by employing this strategy gave a **PCE of 9.28%**.³⁷

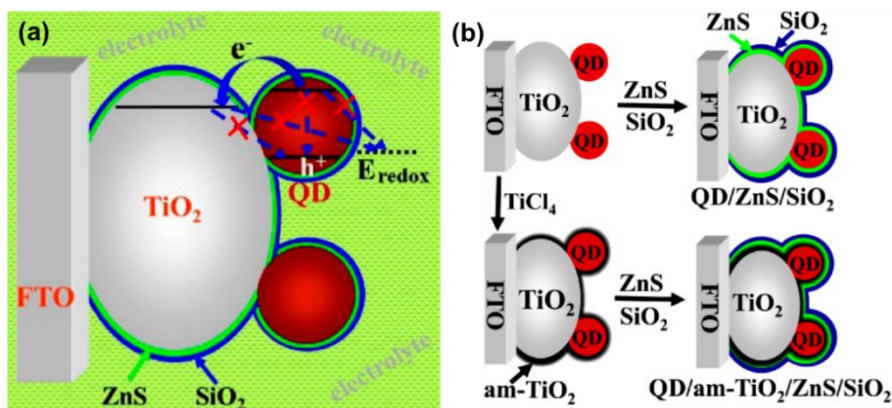


Figure 1.11: Schematic illustration of the mechanism with (a) ZnS/SiO₂ double barrier and (b) am-TiO₂/ZnS/SiO₂ coating inhibiting the charge recombination processes.

Recombination control by metal doping

- Employing an optically active transition metal ion such as Mn²⁺ *creates electronic states in the midgap region of the QD*, and can also help modify the charge separation and recombination dynamics in QDSCs. The d-d transition in the dopant Mn²⁺ is both spin and orbitally forbidden and consequently, *the lifetime is considerably lengthened* to the order of a few microseconds to milliseconds. These long-lived photogenerated charge carriers have been utilized to reduce recombination and thereby improve the efficiency of QDSCs, wherein a cell based on **Mn-doped-CdS/CdSe** was reported to deliver **PCE of 5.4%**.³⁸

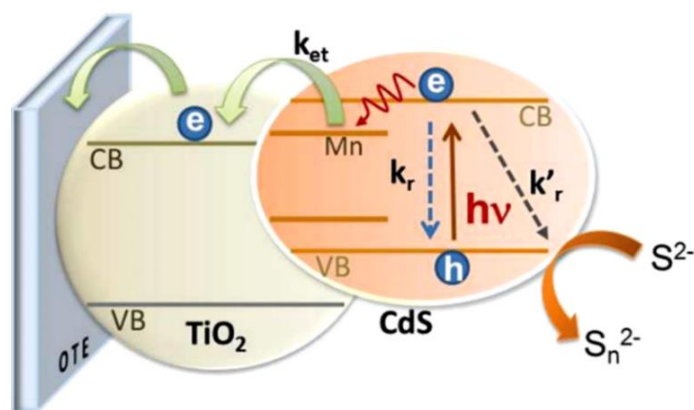


Figure 1.12: Schematic diagram illustrating the electron transfer (k_{et}) from Mn-doped CdS into TiO₂ nanoparticles with k_r and k'_r representing charge recombination.

- ☀ In a modified approach, TiO₂ sensitized with **Mn doped CdSe_{0.65}Te_{0.35}** QDs was passivated by Mn-doped ZnS/SiO₂ passivating layer. The **TiO₂/Mn:QD/Mn:ZnS/SiO₂** system thus constructed showed excellent photovoltaic performance, with the champion cell exhibiting a high **PCE of 9.4%**.³⁹
- ☀ **PbS/Mn-CdS** QDs fabricated on the surface of TiO₂ have given a photoanode with *faster charge transport, more efficient charge separation, resistance to recombination, and excellent stability*. PbS QDs with band gap in NIR have better light-harvesting ability and allow more and more photogenerated charge carriers to accumulate in the conduction band of TiO₂, while the Mn dopant creates new energy states, delaying the exciton recombination time and thus ensuring charge separation. The cell thus constructed by employing these two approaches gave a **PCE of 3.55%**.⁴⁰

Improving charge transfer

TiO₂ receives the injected electrons from photoexcited QDs and provides the conductive pathway from the site of electron injection to the FTO substrate. Therefore, facilitating charge transport by controlling the morphology of TiO₂, including surface orientation, plays an important role in improving the photoconversion efficiency.^{41, 42} TiO₂ electrodes with a higher degree of order may play a vital role in this respect by directing charge separation and electron mobility.

- It has been suggested that TiO₂ nanotube electrodes and TiO₂ inverse opal electrodes will pave the way for considerable enhancement in photovoltaic efficiency of QDSCs.⁴³ **Nanotube arrays** with their *one-dimensional tubular structure, size confinement in the radial direction and high surface area-to-volume ratio*, prove to be superior nanostructures for *separating and directing electrons* to the surface of the collecting electrode. Directionality in the system promotes faster electron transport as the travel time in the TiO₂ electrode is considerably decreased.⁴⁴ Inverse opal TiO₂ electrodes have *large interlinked pores*, allowing increased permeation of quantum dots within the TiO₂ layer, as well as better penetration of the redox couples. **TiO₂ nanotube solar cells sensitized** with CdSe QDs gave an efficiency of **1.8%**, while **TiO₂ inverse opal solar cells** with the same sensitizer gave an efficiency of **3.1%**.⁴³
- Vertically aligned anatase TiO₂ nanowire arrays** with **smooth** and **branched architectures, cosensitized with CdS/CdSe**, were developed as efficient photoanodes for QDSCs. The cell based on branched TiO₂ nanowires showed a high **PCE of 4.20%**, which is 30% greater than that shown by its smooth counterpart. The enhanced photovoltaic performance of the hierarchical TiO₂ nanowire has been attributed to the *long electron lifetime, effective electron injection and prominent charge collection efficiency*, which are consequences of the branched nanowire architecture.⁴⁵
- Another novel photoanode that has been designed is based on **vertically aligned hierarchical TiO₂ nanowire/ZnO nanosheet hybrid arrays**. ZnO is a good alternative to TiO₂ since it has similar band gap (~3.2 eV) and physical properties, and also demonstrates faster electron mobility than TiO₂. On cosensitization with **CdS/CdSe** and utilization of **Cu₂S counter electrode**, this photoanode gave a **PCE of 4.57%**, which may be attributed to the *larger surface area, and increased light harvesting efficiency* of the TiO₂/ZnO heterostructures.⁴⁶

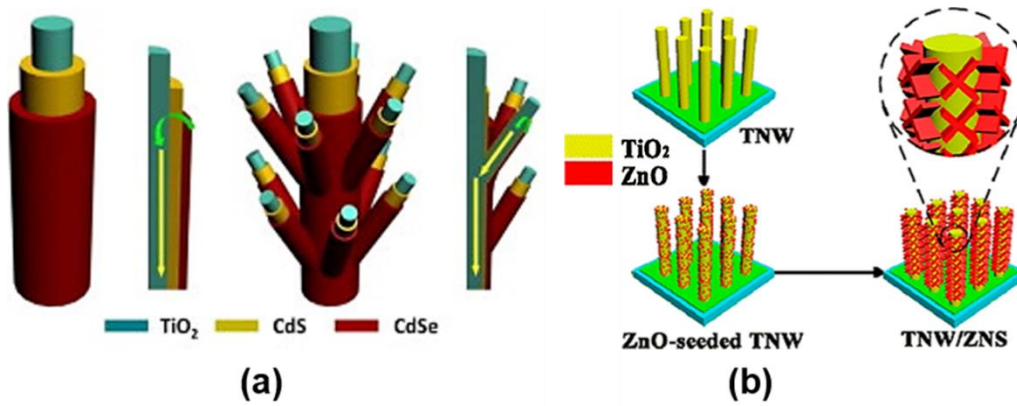


Figure 1.13: Schematic illustration of vertically aligned (a) TiO₂ nanowires with smooth and branched architectures and (b) TiO₂ nanowire/ZnO nanosheet hybrid arrays.

In this work, we have studied four different TiO₂ morphologies with different dimensionalities as possible TiO₂ substrates for Quantum Dot Sensitized Solar Cells. Structures closely resembling zero dimensional TiO₂ nanoparticles, one-dimensional TiO₂ nanowires, two-dimensional TiO₂ nanosheets and three-dimensional TiO₂ nanospheres have been synthesized, and both structural as well as optical characterizations performed. The photovoltaic performance of cells constructed with the CdS-sensitized TiO₂ morphologies as photoanodes were compared in order to analyse the effect of ordered assemblies and directional electron transport on the power conversion efficiency.

2. Experimental Section

2.1 CHEMICALS

Fluorine doped tin oxide (FTO) glass with sheet resistance $25 \Omega \text{ cm}^{-2}$ was purchased from Pilkington and cleaned sequentially in soap solution, 10% HCl solution, 10% NaOH solution, distilled water and acetone/ethanol (v/v 1:1). Degussa TiO₂ P25 (with $50 \pm 15 \text{ m}^2 \text{ g}^{-1}$ surface area) was from Evonik; titanium chloride (TiCl₄), Triton X-100, cadmium acetate [Cd(CH₃COO)₂], sodium sulfide (Na₂S), sodium hydroxide (NaOH, 99%), hydrochloric acid, ammonia, acetonitrile, methanol and ethanol were purchased from Merck; acetyl acetone, anatase TiO₂ powder, titanium (IV) isopropoxide (TIP, 97%), was acquired from Sigma Aldrich; tetra n-propyl ammonium hydroxide (TPAOH, 40%) and tetraethylorthosilicate (TEOS, 98%) were bought from Alfa Aesar. Carbon fabric was procured from Alibaba Pvt. Ltd. Ultra-pure water with a resistivity of $\sim 18.2 \text{ M}\Omega \text{ cm}$ was obtained through Millipore Direct-Q3 UV system.

2.2 SYNTHESIS OF TiO₂ MORPHOLOGIES

2.2.1 Synthesis of TiO₂ Nanowires⁴⁷

TiO₂ nanowires were synthesized by hydrothermal method. 1 g of anatase TiO₂ was placed in a Teflon-lined autoclave of 50 mL capacity, which was filled with 40 mL of 10 M NaOH. The autoclave was then sealed in a stainless steel tank and heated at 160 °C for 24 hours without any disturbance. After the autoclave cooled to room temperature, the sample was washed several times, first with dilute HCl aqueous solution and absolute ethanol, followed by DI water. It was then centrifuged at 5000 rpm for 3 minutes. The sample was dried at 60 °C overnight. White, soft fibrous powder was obtained as the final product.

2.2.2 Synthesis of TiO₂ Nanosheets⁴⁸

Hydrothermal method was employed for the synthesis of TiO₂ nanosheets. 0.1 g of anatase TiO₂ powder and 8 g of tetra n-propyl ammonium hydroxide (TPAOH) were added to 10 mL of 10 M NaOH aqueous solution under stirring. After 30 minutes, the mixture was transferred to a 100 mL Teflon container, sealed in a stainless autoclave and then treated in an air-flow electric oven at 130 °C for 24 hours. After the autoclave cooled to room temperature, the precipitate was collected by centrifugation, and washed with water and ethanol. The sample was then dried in an 60 °C oven. TiO₂ nanosheets were obtained as the final product.

2.2.3 Synthesis of TiO₂ Nanospheres⁴⁹

A colloidal dispersion of Silica particles was first prepared by Stöber method. A mixture of ethanol (10 mL), DI water (~1 M, ~180 mL) and ammonia (~0.2 M, ~37.8 mL) was stirred for 5 minutes, and tetraethylorthosilicate (TEOS, ~0.2 M, ~462 mL) was added to the resulting solution. The reaction was allowed to proceed for 24 hours. The colloidal solution formed was subjected to high-speed centrifugation to obtain silica particles, which were then washed with ethanol three times and dried in an oven at 100 °C for 2 hours. The as-prepared SiO₂ nanoparticles were added to a solution of 3.6 mL of titanium (IV) isopropoxide (TIP), 18 mL of ethanol and 6 mL of acetonitrile. The reaction proceeded via a sol-gel coating process for 6 hours at 4 °C. The resulting SiO₂@TiO₂ Core-Shell Nanoparticles (CSNPs) were isolated by centrifugation, washed with ethanol and DI water. This was followed by calcination at 600 °C for 6 hours, and redispersion in 20 mL of DI water. Chemical etching of the CSNPs was performed by adding an aqueous solution of NaOH (2.5 M, 3.5 mL) to the redispersed solution, and stirring for 6 hours. The TiO₂ HNPs thus formed were separated by centrifugation at 10000 rpm, and washed with ethanol and DI water. TiO₂ hollow nanospheres were obtained as the final product.

2.3 PREPARATION OF PHOTOANODES

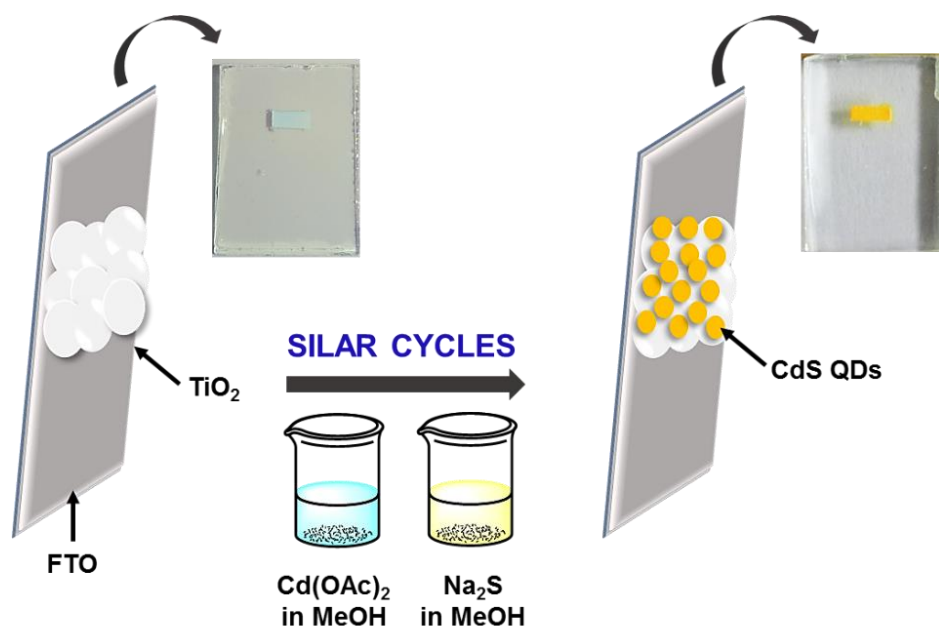


Figure 2.3.1: Schematic representation for preparation of TiO₂/CdS photoanode.

2.3.1 Photoanode Preparation for TiO₂ P25⁵⁰

A TiO₂ paste made of TiO₂ powder (0.3 g) dispersed uniformly in a clear solution of acetylacetone (1.5 mL), ultrapure water (8.5 mL) and Triton X-100 (20 mg) was applied over cleaned FTO-coated conducting glass plates by screen-printing technique. The as-fabricated TiO₂ plates were heated at 60 °C for 30 min, and then annealed at 500 °C for another 30 min. Another layer of TiO₂ was applied using steps detailed above, followed by heating and annealing as performed for the active layer. The TiO₂-coated FTO substrate was then immersed in an aqueous TiCl₄ (40 mM) solution for 30 min at 70 °C, and the resulting TiO₂ film was washed in distilled water, followed by annealing at 500 °C for 30 min.

CdS QDs were deposited over the TiO₂ film by a successive ionic layer adsorption and reaction (SILAR) process. 0.1 M cadmium acetate and 0.1 M sodium sulfide, taken in two separate beakers, were dissolved in methanol, to be used as the cadmium and sulfide precursors, respectively. The TiO₂ films were initially immersed in the cadmium precursor for 2 min, rinsed in methanol to remove excess ions, and then dried in a hot air oven at 60 °C.

The same films were then immersed in the sulfide precursor solution for 2 min followed by rinsing in methanol. This constitutes one SILAR cycle. Six more SILAR cycles were performed, and the resulting film was labelled as a TiO₂/CdS film.

2.3.2 Preparation of photoanode for different TiO₂ morphologies

The active area on the FTO-coated conducting glass plate was wiped with ethanol. The TiO₂ sample was then made into a paste in a mortar and pestle by adding required amounts of acetylacetone and Triton X-100. The as-prepared paste was then applied as a single layer on the active area of the FTO plate. CdS QDs were deposited by 6 cycles of SILAR, as described in Section 2.3.1.

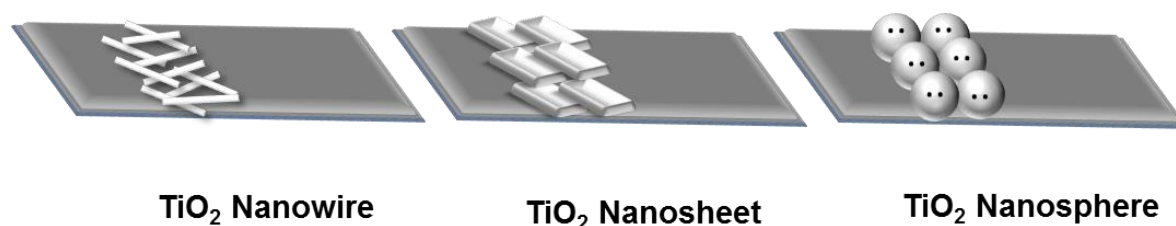


Figure 2.3.2: Schematic representation of different TiO₂ morphologies on FTO.

2.4 ELECTROLYTE AND COUNTER

A clear 0.1 M Na₂S solution in ultrapure water and methanol (mixed in a 3:7 v/v ratio) was used as the polysulfide electrolyte and carbon fabric (sheet resistance ~10 Ω cm⁻²) as the counter electrode.



Figure 2.4: Photograph of carbon fabric pasted on glass.

3. Result and Discussion

3.1 SEM ANALYSIS

The TiO_2 surface morphologies were analysed using Field Emission Scanning Electron Microscopy (FE-SEM, Carl Zeiss AG Supra 40). From the SEM images in Fig. 3.1 (a-d), the different morphologies of TiO_2 have been confirmed. **TiO₂ Nanoparticles (NP)** (3.1a) are seen to have a particulate morphology. They appear as interconnected particles separated by pores, with an average pore size in the range 60-120 nm. **TiO₂ Nanowires (NW)** (3.1b) do not appear as discrete wires but largely in the form of interconnected wires overlapping with each other and forming a mesh-like network. However, in some regions distinct wire like shapes are observed, which are shown in the corresponding inset. **TiO₂ Nanosheets (NSh)** (3.1c) are observed as flaky layers. **TiO₂ Nanospheres (NSp)** (3.1d) appear as interlinked quasi-spherical structures with pores seen on the surface. The porous TiO_2 morphologies allow for facile accommodation of CdS quantum dots.

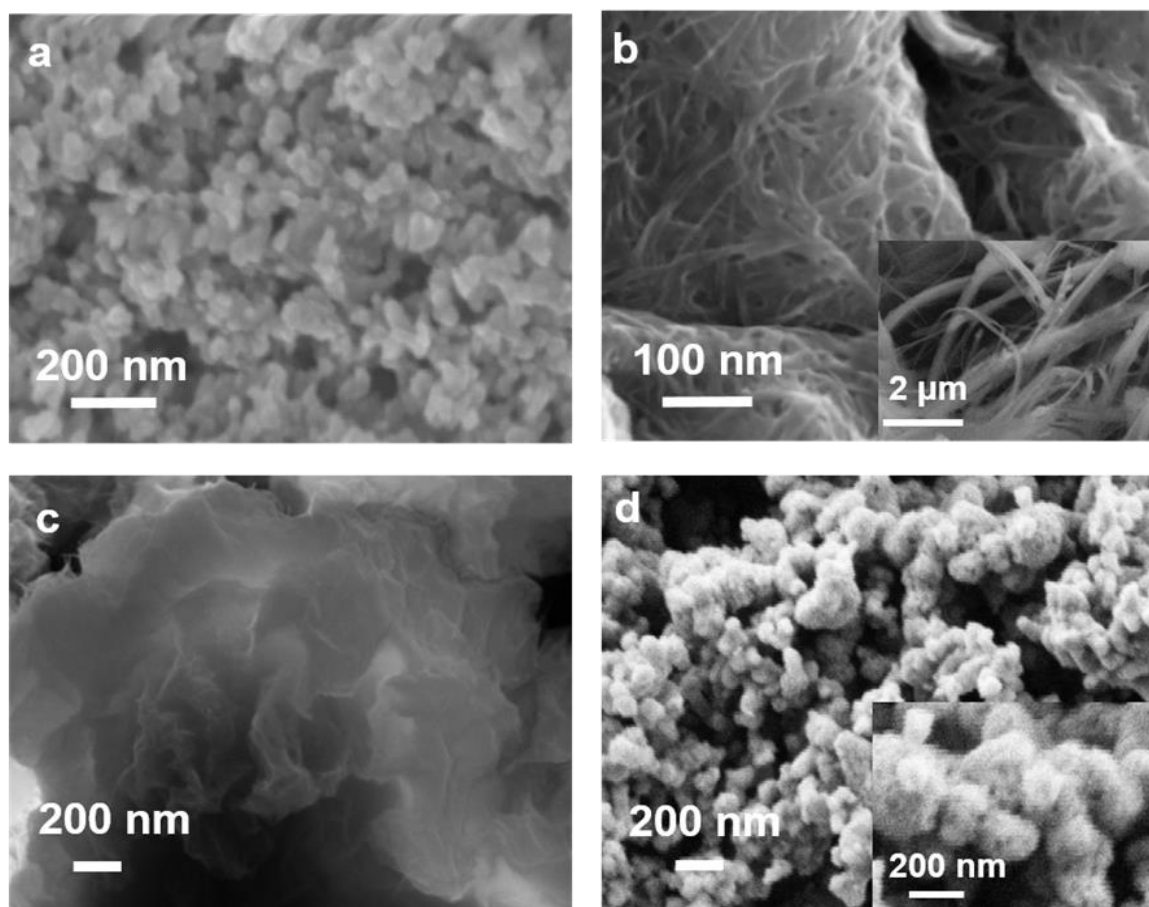


Figure 3.1: SEM Image of (a) TiO_2 NP, (b) TiO_2 NW, (c) TiO_2 NSh and (d) TiO_2 NSp. Insets show the corresponding enlarged view of the different morphologies.

3.2 XRD ANALYSIS

Powder X-ray diffraction measurements were performed using Panalytical X'Pert PRO (reflection $\theta:\theta$ geometry) with Cu $K\alpha$ ($\lambda=1.5406 \text{ \AA}$) radiation, over a 2θ range of 10 to 100° . The three major peaks observed for all the morphologies, including TiO₂ P25, correspond to the (101), (110) and (200) planes of the body centred tetragonal structure of TiO₂ and confirm the anatase structure for TiO₂ (PDF#894203). The broadening of the peaks in the synthesized TiO₂ morphologies (NW, NSh, and NSp) compared to TiO₂ P25 indicate defects and a lower degree of crystallinity in the three samples.

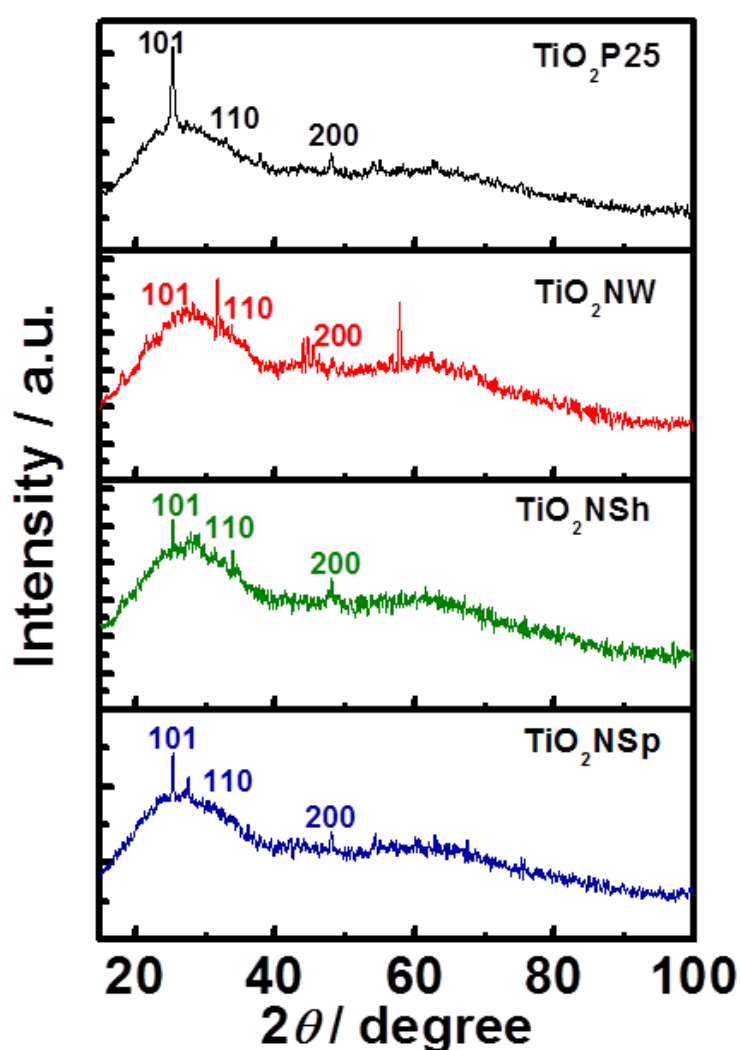


Figure 3.2: X-Ray Diffraction patterns of the different TiO₂ morphologies.

The commercially available TiO₂ P25 as well as the three synthesized TiO₂ morphologies show peaks at similar 2θ values, with corresponding interplanar distances (d-spacing) and lattice planes (hkl indices) as mentioned in Table 3.1

2θ	h k l	d (Å)
25.340	1 0 1	3.517
33.454	1 1 0	2.676
48.037	2 0 0	1.892

Table 3.1: Major peaks with their corresponding hkl and d-spacing values.

3.3 BET AND BJH ANALYSIS

Brunauer–Emmett–Teller (BET) surface area analysis and Barrett-Joyner-Halenda (BJH) pore size and volume analysis were performed using Micromeritics ASAP 2020 Quantachrome instrument under Nitrogen at 77.3 K, after degassing at 300 °C for 3 hours. Fig. 3.3 shows the BET analysis plots, and from the analysis it is deduced that TiO₂ NSh have the highest surface area, followed by TiO₂ NSp, TiO₂ P25 and TiO₂ NW. The data for surface area, pore volume and pore size of the TiO₂ morphologies are listed in Table 3.2. CdS QDs are incorporated within these morphologies, depending on the size and volume of the pores, and the effective available surface area of TiO₂.

Morphology	Surface area (m ² /g)	Pore Volume (cc/g)	Average pore size (Å)
TiO ₂ P25	64.304	0.198	61.786
TiO ₂ NW	61.82	0.227	73.447
TiO ₂ NSp	102.359	0.3107	60.706
TiO ₂ NSh	111.968	0.42	75.04

Table 3.2: BET and BJH analysis data for different TiO₂ morphologies.

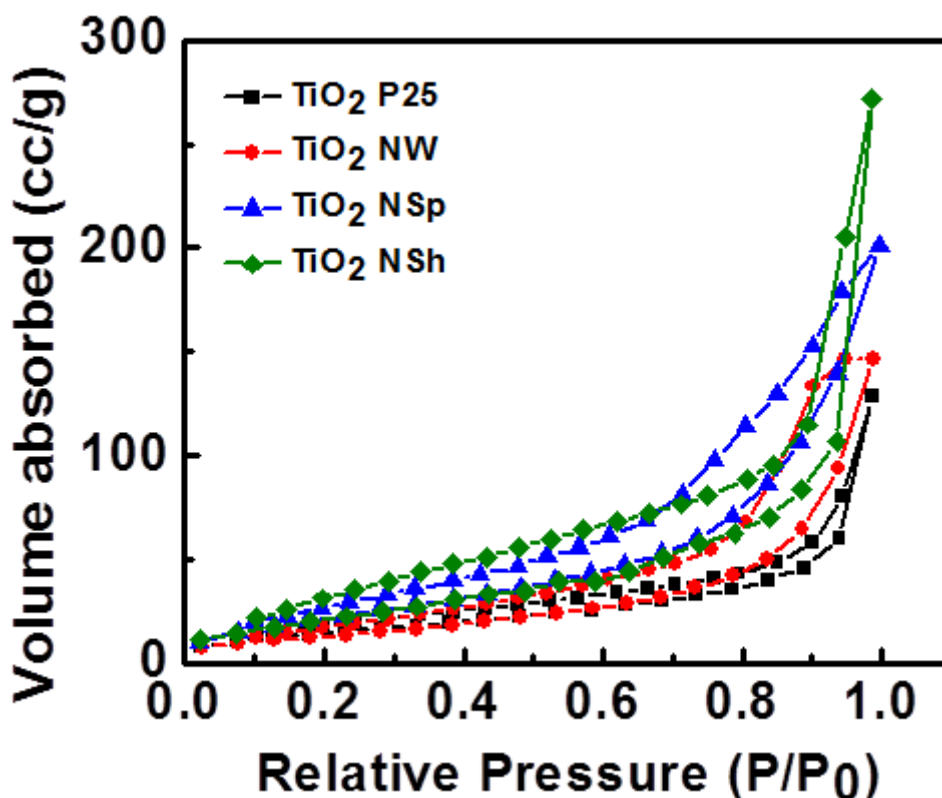


Figure 3.3: BET analysis plots of different TiO₂ morphologies.

3.4 FLUORESCENCE SPECTRAL ANALYSIS

Fluorescence spectra of the different TiO₂ morphologies with CdS QDs were measured on a Horiba Fluoromax-4 fluorescence spectrometer with a filter of 515 nm, as shown in Fig 3.4. From the plot, the intensity of emission of CdS alone was seen to be maximum, followed by TiO₂ NSh/CdS, TiO₂ NSp/CdS, TiO₂ NW/CdS, and was found to be the least for TiO₂ P25/CdS. This indicates that excited electron transfer from the CB of CdS to the CB of TiO₂ is fastest in case of TiO₂ P25, causing significant quenching in the emission of CdS. Lifetime studies, discussed subsequently, further substantiate the emission decrement. The photoexcited electron can follow either of two pathways: it can either get injected into the CB of TiO₂, resulting in a drop in emission, or it can undergo recombination at the band edge or trap states. The quenched luminescence in the former case is suggestive of maximum charge transfer, delivering high photocurrents upon illumination.

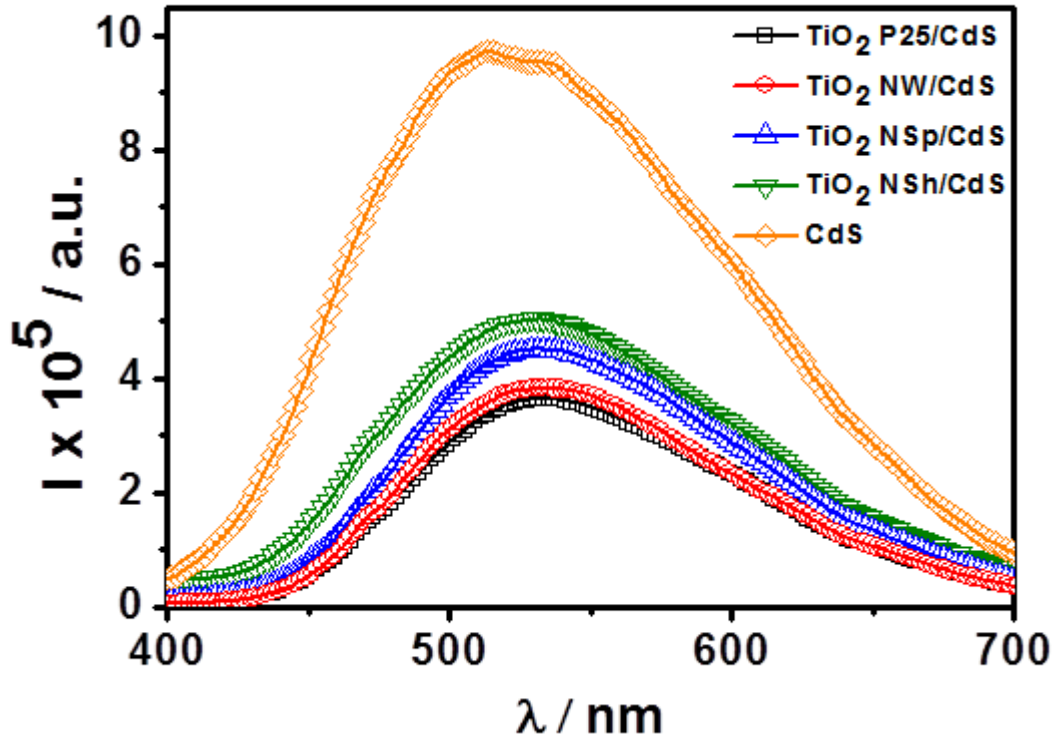


Figure 3.4: Fluorescence spectra of the different TiO₂ morphologies with CdS QDs, and pristine CdS QDs.

3.5 EMISSION DECAY ANALYSIS

Time-correlated single photon counting (TCSPC) method was used for determining emission lifetimes with a Horiba Jobin Yvon data station HUB functioning in the TCSPC mode. A nano LED diode emitting pulses at 370 nm was employed as an excitation source, and the emissions were monitored at a wavelength of 530 nm. The data were fitted to biexponential curves on the basis of χ^2 values, and the fitted parameters are listed in Table 3.3.

The average life time can be determined by using the equation:

$$\langle \tau \rangle = \frac{\sum_i B_i \tau_i^2}{\sum_i B_i \tau_i} ,$$

where τ_i and B_i are decay time constants and amplitudes, respectively, of the individual decay components.

The emission decay lifetime is seen to follow the same order as fluorescence emission, with CdS alone having the longest average lifetime, showing slow decay, and TiO₂ P25/CdS having the shortest lifetime, showing fast decay. This is suggestive of a more efficient charge transfer from CdS to TiO₂ in case of TiO₂ P25, as opposed to recombination, with the charge carriers being rapidly transported to the current collector. For films with CdS QDs anchored to the different TiO₂ morphologies, the lifetimes are comparable, indicating that the nanosized TiO₂, irrespective of the shape, have comparable energy level offsets.

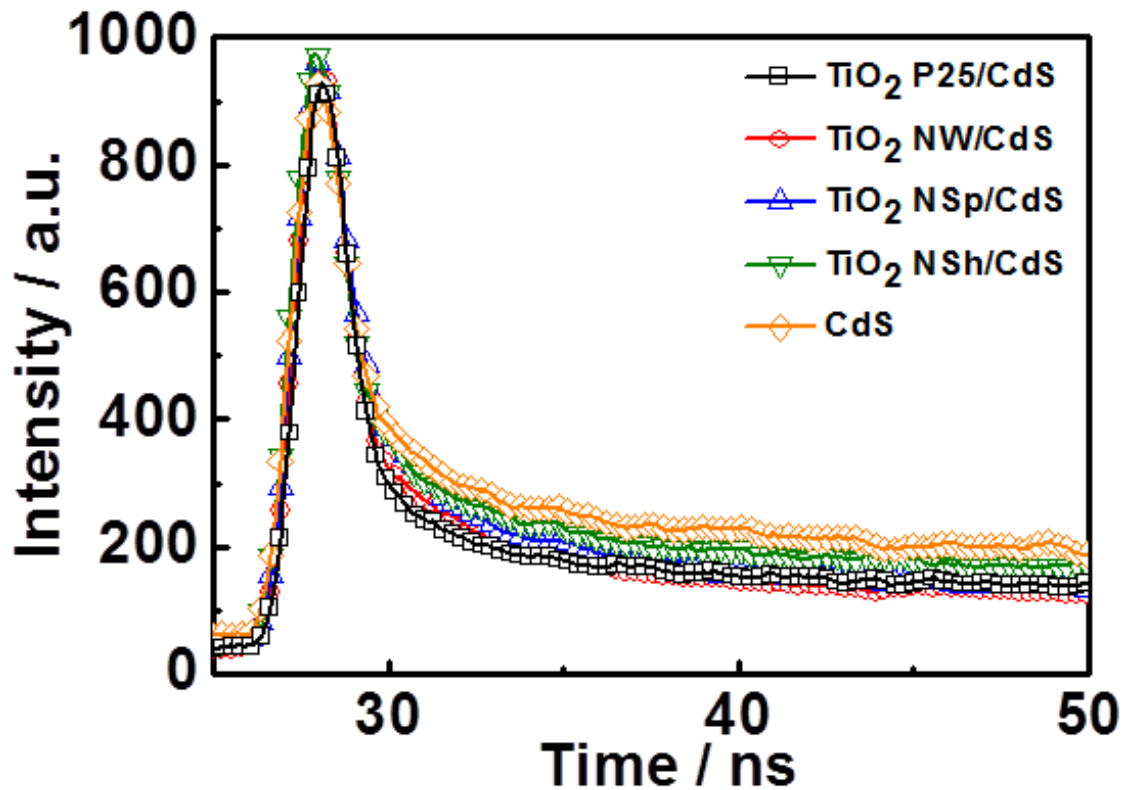


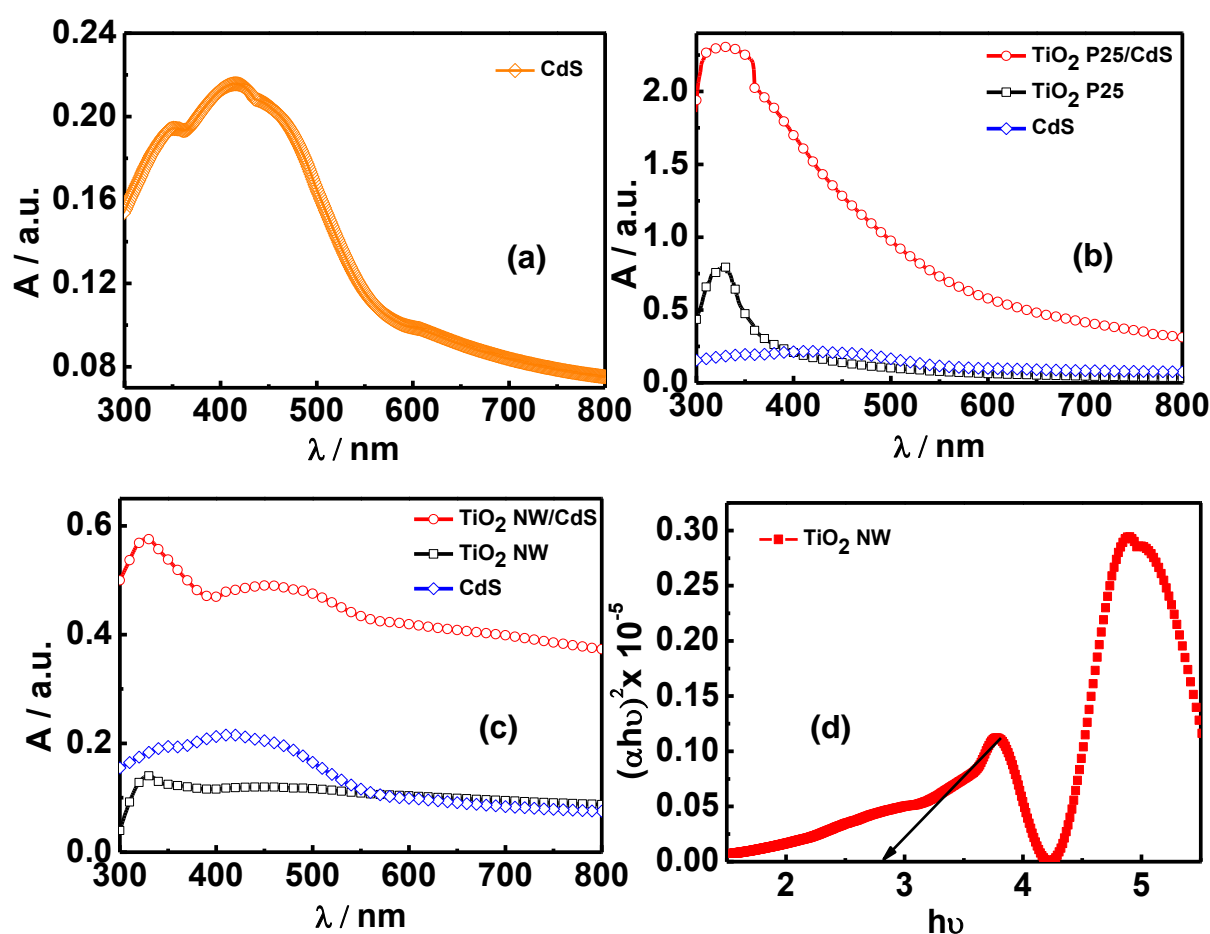
Figure 3.5: Emission decay for the different TiO₂ morphologies with CdS QDs and for pristine CdS QDs.

Sample	B ₁	τ ₁ (ns)	B ₂	τ ₂ (ns)	<τ> (ns)	χ ²
TiO ₂ P25/CdS	19.64	0.00354	80.36	0.553	0.552	1.046535
TiO ₂ NW/CdS	20.45	0.0379	79.55	1.14	1.135	0.975008
TiO ₂ NSp/CdS	99.38	0.00623	0.62	1.78	1.145	0.954900
TiO ₂ NSh/CdS	97.82	0.00615	2.18	1.41	1.182	1.139637
CdS	19.46	0.00944	80.54	4.77	4.770	1.043104

Table 3.3: Kinetic parameters of emission decay analysis deduced from biexponential fits.

3.6 ABSORPTION SPECTRAL ANALYSIS

Optical density analysis was performed in absorbance mode in quartz cuvettes on a UV–VIS–NIR spectrophotometer (Shimadzu UV-3600). CdS QDs alone shows a broad absorption peak at ~400-500 nm, and TiO₂ P25 with CdS also shows an intense peak in the visible range, from which the band gap of both were deduced. However, TiO₂ NW, NSh and NSp were seen to absorb over a wide range of wavelengths in the visible region and consequently, their band gaps could not be inferred directly. Therefore, Tauc plots were used to determine the band gaps of the above morphologies by extrapolation to the abscissa.



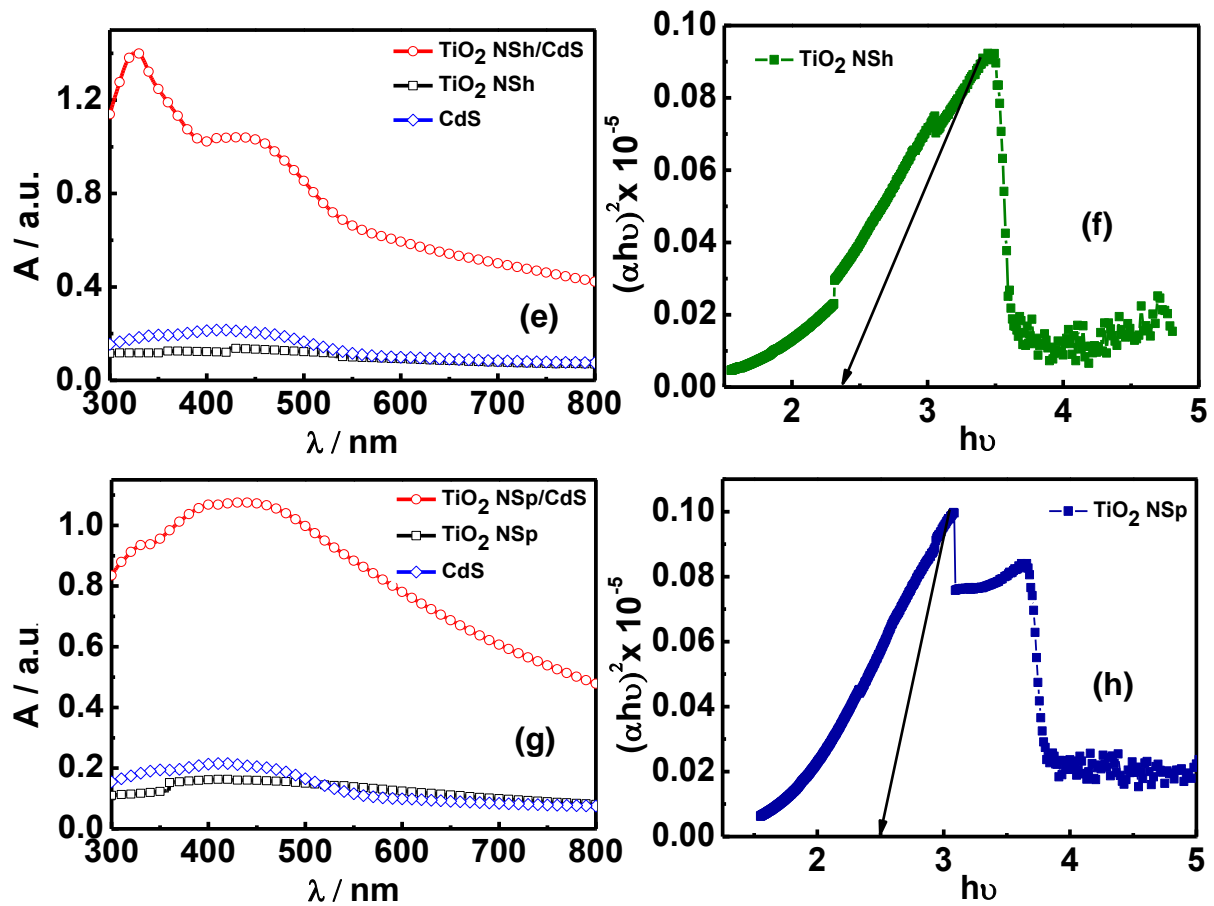


Figure 3.6: Absorption spectra of (a) CdS, (b) TiO₂ P25; (c) TiO₂ NW; (e) TiO₂ NSh; (g) TiO₂ NSp; Tauc plots for (d) TiO₂ NW; (f) TiO₂ NSh; (h) TiO₂ NSp.

Sample	Wavelength (nm)	$\Delta OD = OD(TiO_2/CdS) - OD(TiO_2)$	Band Gap /eV
TiO ₂ P25	400	101.4	3.1
TiO ₂ NW	330-500(broad)	166.4	2.83
TiO ₂ NSp	350-600(broad)	539.5	2.5
TiO ₂ NSh	350-500(broad)	159.2	2.39
CdS	580		2.14

Table 3.4: Wavelength, change in optical density (ΔOD) and band gap data for different TiO₂ morphologies and CdS from absorption spectra and Tauc plots.

3.7 CYCLIC VOLTAMMETRY

Cyclic voltammograms of each different TiO₂ morphology as well as CdS deposited over FTO substrates were recorded in a three electrode cell, with Pt as counter electrode and Ag/AgCl/KCl as reference electrode in an aqueous 0.1 M KCl electrolyte solution, on an Autolab PGSTAT 302N equipped with a NOVA 1.9 software at a scan rate of 20 mV s⁻¹. In each case, a reduction peak was observed in the cathodic sweep, which can be equated to the CB or the Lowest Unoccupied Molecular Orbital (LUMO) position of the sample. This is illustrated in Fig. 3.7.1 and 3.7.2. The electrode potential of the reference is +0.197 V, which is added to the E_{red} vs. Ag/AgCl/KCl to obtain the E_{red} vs. NHE (normal hydrogen electrode) of the respective working electrodes. The E_{red} vs. NHE in volts was subtracted from -4.5 eV (\equiv 0 V versus NHE) in order to convert this value to eV. This data are summarized in Table 3.5.

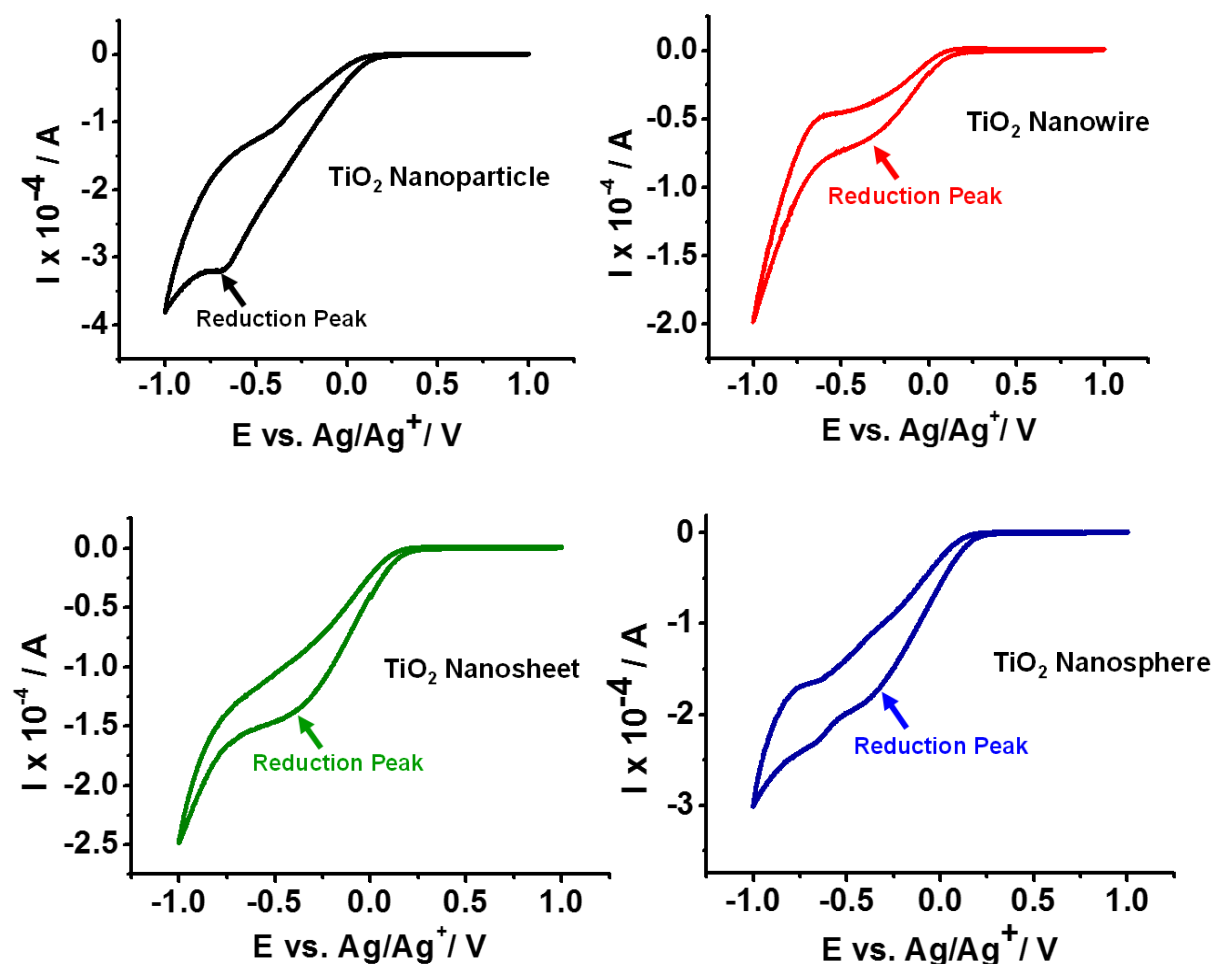


Figure 3.7.1: Cyclic Voltammograms of the different TiO₂ morphologies.

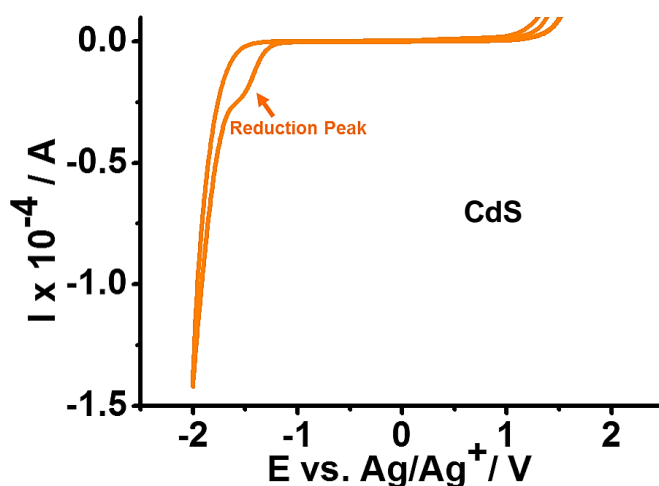


Figure 3.7.2: Cyclic Voltammograms of CdS.

Sample	Reduction Peak (E_{red}) / V	E_{red} (versus NHE) / eV
TiO ₂ P25	-0.68	-4.016
TiO ₂ NW	-0.416	-4.281
TiO ₂ NSp	-0.446	-4.251
TiO ₂ NSh	-0.483	-4.214
CdS	-1.53	-3.167

Table 3.5: Data obtained from Cyclic Voltammograms of different TiO₂ morphologies and CdS.

3.8 IMPEDANCE STUDIES

Impedance measurements were performed on Autolab PGSTAT 302N. The Nyquist plots were generated over a frequency range of 1 MHz to 0.01 Hz, with amplitude 10 mV at zero potential under dark, as seen in Fig 3.8.1. TiO₂ NSh are seen to have the highest impedance over a range of frequencies, indicating high ohmic resistance. The nanospheres offer the least resistance to charge transfer and transport, followed by the nanowires and TiO₂ P25.

Fig. 3.8.2 shows the Bode Phase plot under dark conditions from which the recombination time τ was calculated with the high frequency value. TiO₂ P25 showed the longest recombination time, indicating efficient charge transfer. The recombination times for the other morphologies are listed in Table 3.5.

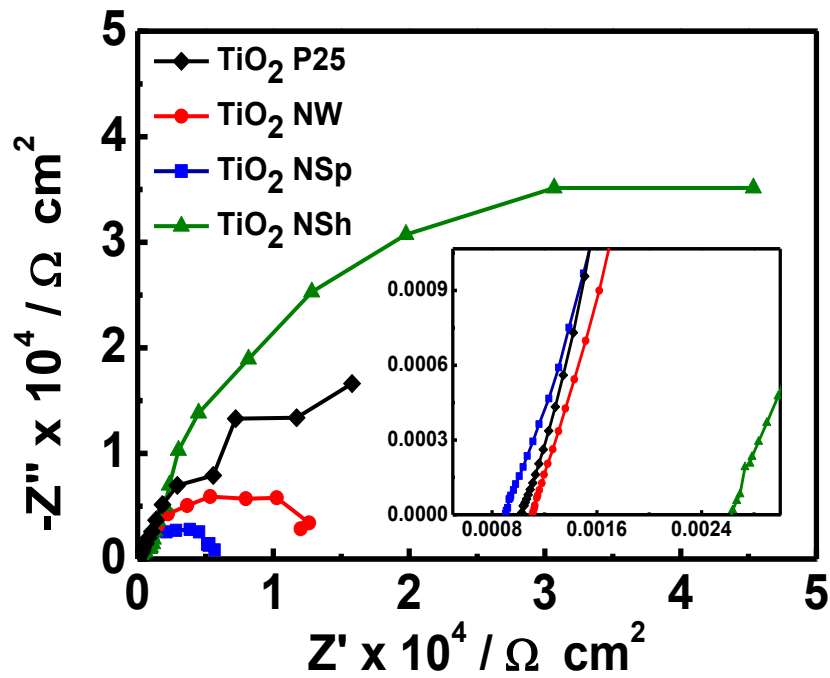


Figure 3.8.1: Nyquist plots for cells with different TiO₂ morphologies;

Inset: enlarged view of the high frequency region.

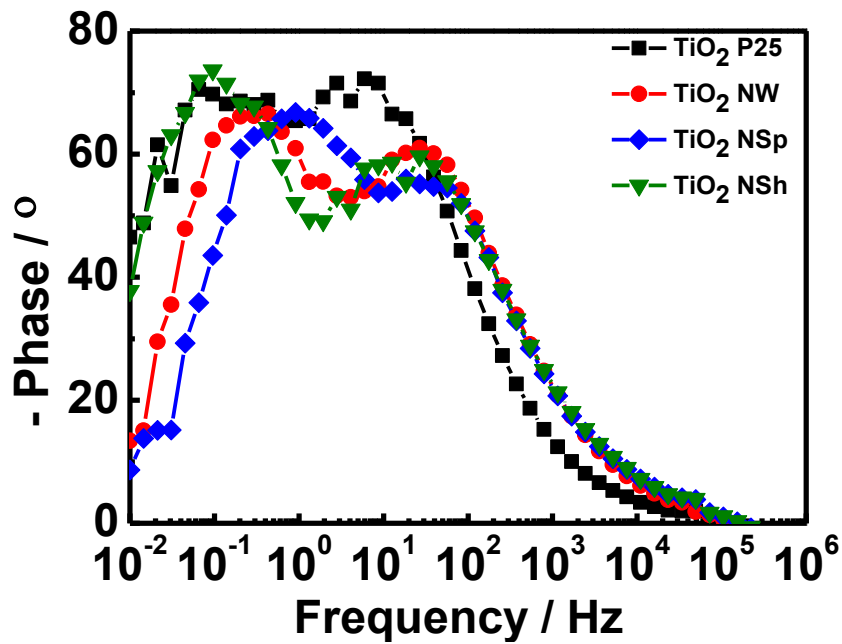


Figure 3.8.2: Bode Phase Plot for different TiO₂ morphologies.

Morphology	f	τ (s)
TiO ₂ P25/CdS	5.825	0.0273
TiO ₂ NW/CdS	26.595	0.00598
TiO ₂ NSp/CdS	18.307	0.00869
TiO ₂ NSh/CdS	27.191	0.00585

Table 3.6: Recombination times for different TiO₂ morphologies.

3.9 ENERGY BAND DIAGRAM

The energy band diagram for different morphologies of TiO₂/CdS showing all possible electron transfer modes on illumination, is illustrated in Fig. 3.8. The positions of VBs and CBs of the different components used in the diagram were determined from cyclic voltammograms and absorption spectra. Additional levels of TiO₂ between the CB of CdS and work function of FTO electronically favour the injection of the photoexcited electron, as shown in the diagram.

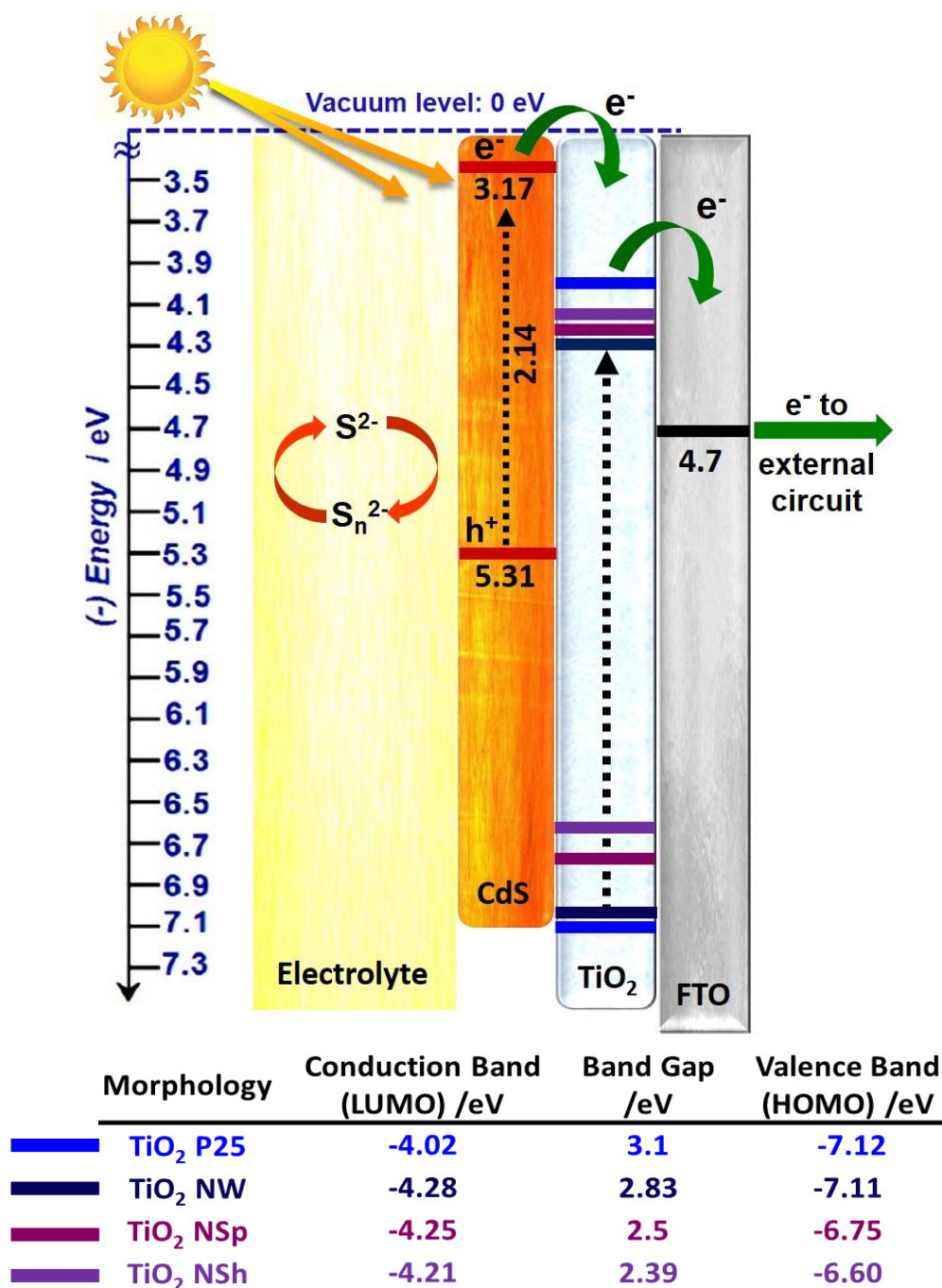


Figure 3.9: Energy band diagram of TiO₂/CdS corresponding to the different morphologies.

3.10 SOLAR CELL CHARACTERIZATION

Solar cell parameters of cells for the different morphologies were measured by considering standard deviation using 0.1 M Na₂S electrolyte, under 1 sun illumination (AM 1.5G, 100 mW cm⁻²) with the listed TiO₂/CdS photoanode and carbon fabric as the counter electrode. The best value of efficiency corresponding to the various TiO₂ morphologies decreases in the order **TiO₂ P25 > TiO₂ NW > TiO₂ NSp > TiO₂ NSh**. J_{sc} and V_{oc} of all the four cells are comparable but lower shunt resistance of the TiO₂ NSh/CdS cell reduces its fill factor making it least proficient.

Sample	Area (cm ²)	J _{sc} (mA cm ⁻²)	V _{oc} (mV)	FF	η _{best} (%)	η _{average} (%)
TiO ₂ P25/CdS	0.0492	11.5433	-0.9021	44.85648	4.671	4.363
TiO ₂ NW/CdS	0.455	9.6201	-0.88745	43.5732	3.720	3.267
TiO ₂ NSp/CdS	0.0341	8.8152	-0.89722	46.70526	3.694	3.279
TiO ₂ NSh/CdS	0.0527	9.4327	-0.86304	36.67945	2.986	2.570

Table 3.7: Solar cell parameters for the different TiO₂ morphologies with CdS.

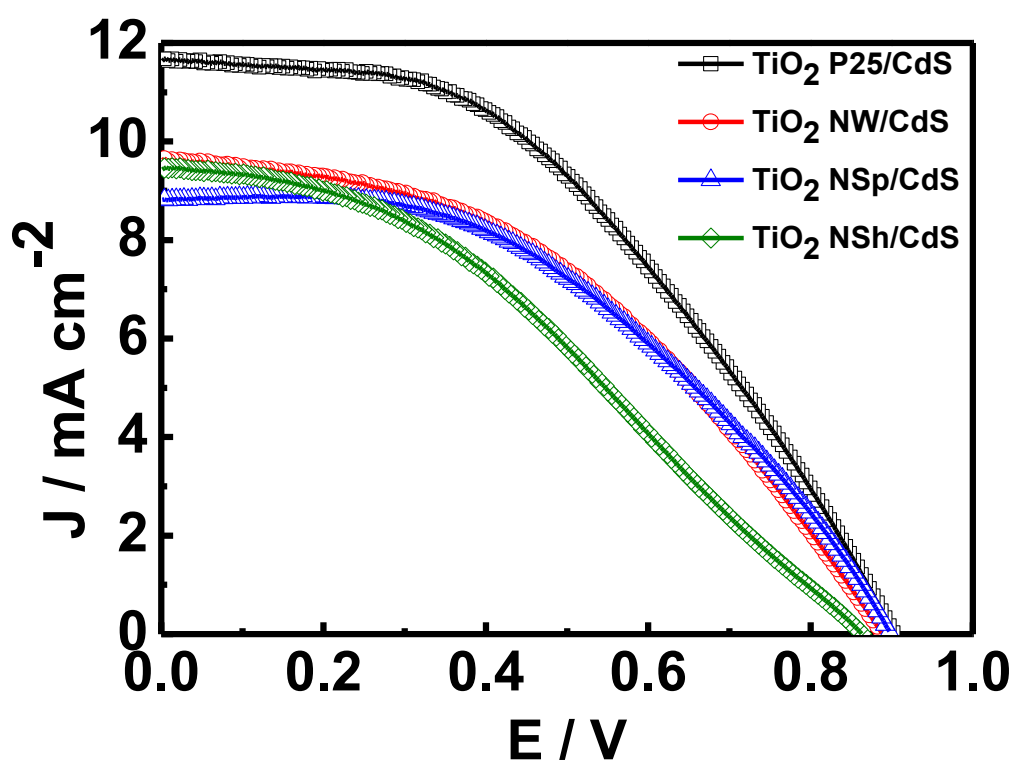


Figure 3.10: J-V curves for different TiO₂ morphologies with CdS.

4. Conclusion

TiO₂ nanoparticles, TiO₂ nanowires, TiO₂ nanosheets and TiO₂ nanospheres were studied as suitable TiO₂ substrates with CdS sensitizer for Quantum Dot Sensitized Solar Cells, with a view to developing ordered assemblies for directing charge transport and increasing electron mobility. Under one sun illumination, the FTO/photoanode/electrolyte assembly with carbon fabric as counter electrode was found to be most efficient for TiO₂ nanoparticles (~4.67%), followed by TiO₂ nanowires (~3.72%), TiO₂ nanospheres (~3.69%) and TiO₂ nanosheets (~2.99%). The shortest lifetime and wide energy band gap obtained from spectral analyses further testify to the highest efficiency of TiO₂ P25, while high impedance of TiO₂ NSh, leading to low photocurrent, is responsible for their least efficiency. TiO₂ NW and NSp show competing values for the various characterizations. While TiO₂ NW promote directional electron transport, the high porosity of TiO₂ NSp promotes high quantum dot loading, giving both morphologies similar boost in photovoltaic performance, resulting in similar trends in power conversion efficiency.

References

1. M. Gratzel, *Phil. Trans. R. Soc. A*, 2007, **365**, 993–1005
2. S. E. Shaheen, D. S. Ginley and G. E. Jabbour, *MRS Bulletin*, 2005, **30**, 10-19
3. P.V. Kamat, *J. Phys. Chem. C*, 2008, **112**, 18737–18753
4. M. A. Green, K. Emery, Y. Hishikawa, W. Warta and E. D. Dunlop, *Prog. Photovolt: Res. Appl.*, 2012, **20**, 12–20
5. W. H. Bloss, F. Pfisterer, M. Schubert and T. Walter, *Prog. Photovolt: Res. Appl.*, 1995, **3**, 3–24
6. M. A. Green, *Physica E*, 2002, **14**, 65 – 70
7. W. Shockley and H. J. Queisser, *J. Appl. Phys.*, 1961, **32**, 510–519.
8. X. Wang, G. I. Koleilat, J. Tang, H. Liu, I. J. Kramer, R. Debnath, L. Brzozowski, D. A. R. Barkhouse, L. Levina, S. Hoogland and E. H. Sargent, *Nat. Photonics*, 2011, **5**, 480–484
9. E.H. Sargent, *Nat. Photonics*, 2009, **3**, 325–331.
10. B. O'Regan and M. Gratzel, *Nature*, 1991, **353**, 737 – 743
11. M. Gratzel, *Inorg. Chem.*, 2005, **44**, 6841-6851
12. A. Yella, H.W. Lee, H. N. Tsao, C. Yi, A. K. Chandiran, M.K. Nazeeruddin, E. Wei-Guang Diao, C. Y. Yeh, S. M. Zakeeruddin, M. Grätzel, *Science*, 2011, **334**, 629–634.
13. S. Mathew, A. Yella, P. Gao, R. Humphry-Baker, B. F. E. Curchod, N. Ashari-Astani, I. Tavernelli, U. Rothlisberger, M. K. Nazeeruddin and M. Grätzel, *Nat. Chem.*, 2014, **6**, 242–247
14. P. V. Kamat, *J. Phys. Chem. Lett.*, 2013, **4**, 908–918
15. P. V. Kamat, K. Tvrđy, D. R. Baker and J. G. Radich, *Chem. Rev.*, 2010, **110**, 6664–6688
16. J. M. Luther, J. Gao, M. T. Lloyd, O. E. Semonin, M. C. Beard and A. J. Nozik, *Adv. Mater.*, 2010, **22**, 3704–3707
17. N. P. Benekohal, V. González-Pedro, P. P. Boix, S. Chavhan, R. Tena-Zaera, G. P. Demopoulos and I. Mora-Seró, *J. Phys. Chem. C*, 2012, **116**, 16391
18. X. Y. Yu, J. Y. Liao, K. Q. Qiu, D. B. Kuang, and C. Y. Su, *ACS Nano*, 2011, **5**, 9494.
19. G. Zhu, L. Pan, T. Xu and Z. Sun, *ACS Appl. Mater. Interfaces*, 2011, **3**, 1472.
20. H. Lee, M. Wang, P. Chen, D. R. Gamelin, S. M. Zakeeruddin, M. Grätzel and M. K. Nazeeruddin, *Nano Lett.*, 2009, **9**, 4221.

21. A. J. Nozik, *Chemical Physics Letters*, 2008, **457**, 3–11
22. V. Chakrapani, D. Baker and P. V. Kamat, *J. Am. Chem. Soc.*, 2011, **133**, 9607–9615
23. K. Zhao, Z. Pan and X. Zhong, *J. Phys. Chem. Lett.*, 2016, **7**, 406–417
24. J. Duan, H. Zhang, Q. Tang, B. He and L. Yu, *J. Mater. Chem. A*, 2015, **3**, 17497–17510
25. I. Hwang and K. Yong, *ChemElectroChem*, 2015, **2**, 634–653.
26. A. G. Kontos, V. Likodimos, E. Vassalou, I. Kapogianni, Y. S. Raptis, C. Raptis and P. Falaras, *Nanoscale Res. Lett.*, 2011, **6**, 1–6
27. J. Yang, J. Wang, K. Zhao, T. Izuishi, Y. Li, Q. Shen and X. Zhong, *J. Phys. Chem. C*, 2015, **119**, 28800–28808
28. J. Wang, I. Mora-Seró, Z. Pan, K. Zhao, H. Zhang, Y. Feng, G. Yang, X. Zhong and J. Bisquert, *J. Am. Chem. Soc.*, 2013, **135**, 15913–15922
29. Z. Pan, K. Zhao, J. Wang, H. Zhang, Y. Feng and X. Zhong, *ACS Nano*, 2013, **7**, 5215–5222
30. Z. Pan, I. Mora-Seró, Q. Shen, H. Zhang, Y. Li, K. Zhao, J. Wang, X. Zhong and J. Bisquert, *J. Am. Chem. Soc.*, 2014, **136**, 9203–9210
31. C. Ratanatawanate, C. Xiong and K. J. Balkus, *ACS Nano*, 2008, **2**, 1682–1688.
32. B. R. Hyun, Y. W. Zhong, A. C. Bartnik, L. Sun, H. D. Abruña, F. W. Wise, J. D. Goodreau, J. R. Matthews, T. M. Leslie and N. F. Borrelli, *ACS Nano*, 2008, **2**, 2206–2212.
33. V. González-Pedro, C. Sima, G. Marzari, P. P. Boix, S. Giménez, Q. Shen, T. Dittrich and I. Mora-Seró, *Phys. Chem. Chem. Phys.*, 2013, **15**, 13835–13843
34. K. Zhao, H. Yu, H. Zhang, and X. Zhong, *J. Phys. Chem. C*, 2014, **118**, 5683–5690
35. J. Du, X. Meng, K. Zhao, Y. Li and X. Zhong, *J. Mater. Chem. A*, 2015, **3**, 17091–17097
36. K. Zhao, Z. Pan, I. Mora-Seró, E. Cánovas, H. Wang, Y. Song, X. Gong, J. Wang, M. Bonn, J. Bisquert and X. Zhong, *J. Am. Chem. Soc.*, 2015, **137**, 5602–5609
37. Z. Ren, J. Wang, Z. Pan, K. Zhao, H. Zhang, Y. Li, Y. Zhao, I. Mora-Seró, J. Bisquert and X. Zhong, *Chem. Mater.*, 2015, **27**, 8398–8405
38. P. K. Santra and P. V. Kamat, *J. Am. Chem. Soc.*, 2012, **134**, 2508–2511
39. J. Wang, Y. Li, Q. Shen, T. Izuishi, Z. Pan, K. Zhao and X. Zhong, *J. Mater. Chem. A*, 2016, **4**, 877–886

40. H. J. Kim, H. D. Lee, C. S. S. P. Kumar, S. S. Rao, S. H. Chung and D. Punnoose, *New J. Chem.*, 2015, **39**, 4805-4813
41. N.G. Park, J. Van de Lagemaat and A. J. Frank, *J. Phys. Chem. B*, 2000, **104**, 8989-8994.
42. A. Kongkanand, K. Tvrdy, K. Takechi, M. Kuno and P. V. Kamat, *J. Am. Chem. Soc.*, 2008, **130**, 4007-4015
43. T. Toyoda and Q. Shen, *J. Phys. Chem. Lett.*, 2012, **3**, 1885-1893
44. K. Zhu, N. R. Neale, A. Miedaner and A. J. Frank, *Nano Lett.*, 2007, **7**, 69-74
45. H. S. Rao, W. Q. Wua, Y. Liub, Y. F. Xua, B. X. Chena, H. Y. Chena, D. B. Kuanga and C. Y. Sua, *Nano Energy*, 2014, **8**, 1-8
46. H. L. Feng, W. Q. Wu, H. S. Rao, Q. Wan, L. B. Li, D. B. Kuang and C. Y. Su, *ACS Appl. Mater. Interfaces*, 2015, **7**, 5199-5205
47. Y. X. Zhang, G. H. Li, Y. X. Jin, Y. Zhang, J. Zhang and L. D. Zhang, *Chemical Physics Letters*, 2002, **365**, 300–304
48. M. Leng, Y. Chen and J. Xue, *Nanoscale*, 2014, **6**, 8531-8534
49. J. Yun, S. H. Hwang and J. Jang, *ACS Appl. Mater. Interfaces*, 2015, **7**, 2055-2063
50. P. N. Kumar, M. Deepa and P. Ghosal, *ACS Appl. Mater. Interfaces*, 2015, **7**, 13303-13313